Master's thesis

NTNU
Norwegian University of Science and Technology
Faculty of Natural Sciences
Department of Physics

Lise Eder Murberg

The secondary ozone layer and energetic particle precipitation

Master's thesis in Applied Physics and Mathematics
Supervisor: Patrick Joseph Espy
Co-supervisor: Yvan Joseph Orsolini
June 2022

NTNU
Norwegian University of
Science and Technology

Lise Eder Murberg

The secondary ozone layer and energetic particle precipitation

Master's thesis in Applied Physics and Mathematics
Supervisor: Patrick Joseph Espy
Co-supervisor: Yvan Joseph Orsolini
June 2022

Norwegian University of Science and Technology
Faculty of Natural Sciences
Department of Physics

NTNU
Norwegian University of
Science and Technology

Abstract

The secondary ozone layer is a global peak in ozone abundance in the upper mesosphere-lower thermosphere (UMLT) around 90-100 km. At this altitude ozone is easily photodissociated during daytime, making the ozone mixing ratio larger in nighttime. Nighttime ozone in chemical equilibrium is governed by temperature and species such as atomic oxygen and atomic hydrogen, which acts as chemical sources and sinks. Energetic particle precipitation (EPP) from heliophysical and geomagnetic processes is known to influence the primary (stratospheric) and tertiary (mesospheric) ozone layers, but the effect of EPP on UMLT ozone has not yet been studied. This study uses NASA's Microwave Limb Sounder (MLS) nighttime ozone volume mixing ratio (VMR), nighttime CO VMR and temperature compared to daily Ap indices, which indicates the level of geomagnetic activity in the atmosphere. Carbon monoxide (CO) has been used as a tracer of the dynamical changes in the UMLT. The SD-WACCM-X model has been used to study residual circulation effects from EPP in the UMLT. MLS V5.0 is compared to MLS V4.2X at 0.002 hPa, showing the improvements of nighttime O_3 VMR in MLS V5.0. The natural variations due to seasons, temperature and dynamical effects is studied at 0.001 hPa for MLS V5.0. Seasonal zonal-means of ozone VMR at high and low Ap show an ozone enhancement at high latitudes for winter seasons. For transitional seasons (MAM and SON) at high latitudes there is an ozone depletion for late autumn and an ozone enhancement for early spring. SD-WACCM-X results show that EPP affects the residual circulation and thus affecting ozone through transport and temperature effects. A case study analysis of 7-10. Nov 2004 and a Superposed Epoch Analysis (SEA) of DJF further support the conclusion that the meridional circulation leads to temperature and composition changes which influence the secondary ozone layer.

Sammendrag

Det sekundære ozonlaget er det globale toppunktet av ozon i øvre mesosfære-nedre termosfære (UMLT) rundt 90-100 km. Ved denne høyden fotodissosieres ozon lett på dagtid, noe som gjør at blandingsforholdet av ozon er større om natten. Ved kjemisk likevekt er ozon om natten styrt av temperatur og kjemiske arter som atomært oksygen og atomært hydrogen, som fungerer som kilder og synker. Energisk partikkelnedbør (EPP) fra heliofysiske og geomagnetiske prosesser er kjent for å påvirke det primære- (stratosfæriske) og det tertiære (mesosfæriske) ozonlaget, men effekten av EPP for UMLT ozon er ennå ikke studert. Denne studien bruker NASAs Microwave Limb Sounder (MLS) ozon volumsblandingsforhold (VMR) på natten, CO VMR på natten og temperatur sammenlignet med daglig Ap-indeks, som indikerer nivået av geomagnetisk aktivitet i atmosfæren. Karbonmonoksid (CO) har blitt brukt som en sporer av dynamiske endringer i UMLT. Modellen SD-WACCM-X har blitt brukt til å studere sirkulasjonseffekter fra EPP i UMLT. MLS V5.0 har blitt sammenlignet med MLS V4.2X ved trykknivå 0,002 hPa, og viser forbedringene i nattlig O_3 VMR for MLS V5.0. De naturlige variasjonene på grunn av årstider, temperatur og dynamiske effekter er studert ved 0,001 hPa for MLS V5.0. Sesongmessige lengdegrads-gjennomsnitt for ozon VMR ved høy og lav Ap viser en ozon-økning for høye breddegrader i vintersesongene. I overgangssesongene (MAM og SON) for høye breddegrader er det en ozon-nedbrytning for sen høst og en ozon-forsterkning for tidlig vår. Resultated fra SD-WACCM-X viser at EPP påvirker sirkulasjonen og dermed påvirker ozon gjennom transport- og temperatureffekter. En eksempelstudie av 7-10. Nov 2004 og en overlagt-epokeanalyse (SEA) av DJF fører videre til konklusjonen at meridionalsirkulasjonen fører til temperatur- og sammensetningsendringer som påvirker det sekundære ozonlaget.

Preface

The work presented is the final master thesis of the study program Applied Physics and Mathematics at the Norwegian University of Science and Technology (NTNU). The thesis is carried out at the Department of Physics under the supervision of Professor Patrick J. Espy and Professor Yvan J. Orsolini.

First, I express my sincere gratitude to Prof. Patrick J. Espy and Prof. Yvan J. Orsolini for allowing me to conduct this research under their supervision. Thank you both for all the good discussions, helpful insights, and your enthusiasm toward the project. I would like to especially thank Patrick for his insights on working with atmospheric data and the physics of the atmosphere and show my gratitude to Yvan for his great knowledge on ozone chemistry and atmospheric models. The combination of these two supervisors made working on the thesis even more exciting and educational. Furthermore, I would also like to thank:

- Tiril Løvset for all our detailed discussions about the project, work sessions and cafeteria lunches throughout the last year. Our friendship and professional relationship means a lot.
- PhD. Jia Jia her great feedback and suggestion during all our weekly meetings.
- Dong Wu, Jae N. Lee and Jude Salinas from NASAs Goddard team for listening to my presentation on the thesis and supplying new suggestions to the project.
- Student advisor Brit Wenche Meland for guiding me through 5 years of studying.

Table of Contents

Abbreviations

UMLT	=	Upper Mesosphere-Lower Thermosphere
EPP	=	Energetic Particle Precipitation
NASA	=	National Aeronautics and Space Administration
VMR	=	Volume Mixing Ratio
CO	=	Carbon monoxide
WACCM	=	Whole Atmosphere Community Climate Model
MLS	=	Microwave Limb Sounder
DJF	=	December, January, February
MAM	=	March, April, May
JJA	=	June, July, August
SON	=	September, October, November
SEA	=	Superposed Epoch Analysis
UV	=	Ultraviolet
MLT	=	Mesosphere-Lower Thermosphere
MEE	=	Medium-Energy Electrons
FAI	=	Fédération Aéronautique Internationale
EUV	=	Extreme ultraviolet
SEP	=	Solar energetic particles
SPE	=	Solar Proton Event
EOS	=	Earth Observing System
Kp	=	Planetariche Kennziffe
Ap	=	Averaged planetary
AE	=	Auroral Electrojet
Dst	=	Disturbance storm time
MC	=	Monte Carlo
CESM	=	Community Earth System Model
NCAR	=	National Center for Atmospheric Research
TIE-GCM	=	Thermosphere-Ionosphere-Electrodynamics General Circulation Model
MERRA	=	Modern-Era Retrospective Analysis for Research and Application
NH	=	Northern Hemisphere
SH	=	Southern Hemisphere
SAO	=	Semiannual oscillation

Chapter 1

Introduction

There are three known regions of ozone abundance in the Earth's atmosphere which are the primary ozone layer in the stratosphere, the tertiary ozone layer in the mesosphere and the secondary ozone layer in the upper mesosphere-lower thermosphere (UMLT). The peak ozone abundance in the secondary ozone layer lies near 90 - 100 km. At this altitude ozone is more abundant in nighttime, due to its easily photo-dissociated nature in daytime. The abundance of nighttime ozone in its state of chemical equilibrium is governed by temperature and the longer-lived species of atomic hydrogen and oxygen, which acts as chemical sources and sinks. The ozone abundance is dependent on the diurnal variability, which has strong connections to UV radiation and atmospheric tides (Smith et al., 2005). The secondary ozone layer is affected by solar radiative variability through solar UV irradiance which is demonstrated through the 11-year solar cycle, and the more rapid 27-day solar rotation cycle (Lee et al., 2016).

Energetic particle precipitation (EPP) refers to highly energetic electrons, protons, neutrons, and ions that are accelerated to the atmosphere through heliophysical and geomagnetic processes. In the UMLT, auroral electron precipitation occurs routinely down to about 90 km while Medium-energy electrons (MEE) from sporadic geomagnetic storms can penetrate further into the mesosphere. Electron precipitation leads to neutral and ionic reactions that alter the background chemistry of the atmosphere. In the primary and tertiary ozone layers it has already been established that energetic particle precipitation leads to an ozone depletion at high latitudes in the winter hemisphere (Aikin et al., 1999). The impact of EPP on the secondary ozone layer has not yet been fully explored, however idealized simulations by Guttu et al. (2020) using the NCAR Whole Atmosphere Community Climate Model (WACCM) indicate that MEE leads to an ozone depletion in the secondary layer of up to 0.15 ppmv or 3.5% in northern high latitudes during winter. This effect is so far only studied with simulations, and it is unclear if the effect is due to changes in the chemical sources and sinks of ozone or indirect effects due to changes in circulation and temperature.

This thesis aims to quantify the ozone variability in the secondary layer associated with energetic particle precipitation by comparing the newest version (V5.0) of data from NASA's Microwave Limb Sounder (MLS) (Schwartz et al., 2021) with the Ap daily index retrieved from GFZ German Research Centre for Geoscience (Matzka, Bronkalla et al.,

2021). Several methods have been used to analyse the effects of EPP on the secondary ozone layer.

Firstly, MLS V5.0 and MLS 4.2X were compared at 0.002 hPa to confirm the validity and improvements of MLS V5.0 as it is a brand new version of the data set. Then the climatological effects in nighttime ozone, temperature and nighttime CO for MLS V5.0 were studied at the secondary ozone layer at 0.001 hPa, together with the correlation between the species. To ascertain the effect of EPP on the UMLT ozone I examined the zonal-mean variability at high and low values of an EPP index, Ap, as a function of season. Both a case study of the geomagnetic event of 7-10. Nov 2004 and a climatological study using Superposed Epoch Analysis were used. Significance levels of the results were determined using a Monte Carlo bootstrapping method, and comparisons were made with the modelled SD-WACCM-X residual circulation results to examine possible dynamics effects on the UMLT ozone.

Chapter 2

Theory

This chapter aims to provide a theoretical overview of the concepts relevant this project, to better understand the results presented later on. Firstly, a review of the Earth's atmosphere with focus on composition, structure and circulation will be provided. Then the chemistry behind the secondary ozone layer and CO as a dynamical tracer is explained. Lastly, a description of energetic particle precipitation (EPP) is given, with details of the solar proton event of 7-10. Nov 2004 and EPPs effect on ozone.

2.1 The atmosphere

The Earth's atmosphere is the layer of gases surrounding the planet and retained by Earth's gravity. In this layer a variety of physical processes takes place which are essential to all life. Atmospheric layers provide pressure for liquid water to exist on the surface, absorb ultraviolet (UV) solar radiation and provide a livable climate through the greenhouse effect. The mesosphere-lower thermosphere (MLT) is defined as the region of the atmosphere between 60 and 110 km in altitude, and constitutes what is referred to as the middle atmosphere. This region is very interesting due to its position between a dynamical and well mixed atmosphere below, and an ionized atmosphere where molecular diffusion dominate above. This section is based on Andrews (2010) and will give a brief view of the characteristics of the atmosphere in general, with focus on the MLT specifically.

2.1.1 Atmospheric composition

The atmosphere consists of a mixture of ideal gases. Table 2.1 gives an overview of the constituents of the Earth's atmosphere. Major constituents such as molecular nitrogen and molecular oxygen dominate by volume, but minor constituents such as carbon dioxide, water vapour and ozone also play crucial roles in the atmospheric chemistry due to their ability to absorb and emit infra-red radiation. The gases are defined by their abundance and lifetime in a system. The most common way of expressing the amount of a gas in

Gas	Formula	Concentration
Nitrogen	N_2	78.08%
Oxygen	O_2	20.95%
Argon	Ar	0.93%
Water vapour*	H_2O	0-4%
Carbon dioxide	CO_2	420 ppmv
Neon	Ne	18.18 ppmv
Helium	He	5.24 ppmv
Methane	CH_4	1.79 ppmv
Krypton	Kr	1.14 ppmv
Hydrogen	H_2	0.53 ppmv
Nitrous oxide	N_2O	0.325 ppmv
Carbon-monoxide	CO	∼0.2 ppmv
Xenon	Xe	0.087 ppmv
Ozone	O_3	∼0.6 ppmv
Nitrogen-dioxide	NO_2	∼0.2 ppmv

Table 2.1: Main constituents of dry atmosphere with percent by volume. *Concentration of water vapour is not included in dry atmosphere.

a system is concentration (kg m^3) and volume mixing ratios (m^3 gas per m^3 air). Minor constituents are often given in units of parts per million volume (ppmv). The constituents in table 2.1 vary with altitude. The lower 5 km of the atmosphere contain ∼90% of all water vapour, while the majority of ozone is found above 30 km. The turbopause at around 100 km marks the hypothetical boundary between the well mixed atmosphere known as the homosphere, and the domain where diffusive separation dominates known as the heterosphere.

2.1.2 Vertical structure

There are five main regions in the atmosphere, where each region is distinguished from each other by the vertical temperature profile. The vertical profile as given by MLS V5.0 in 2020 is shown in Figure 2.1 with vertical axis as pressure and an approximate altitude given by the US standard atmosphere. The boundary layers between the regions, as shown by red lines, are given by a change in the sign of the temperature gradient and vary with season and latitude. The lowest layer is called the troposphere. About 80 % of the atmosphere is contained within this layer and the region is on average just 15 km thick. This region is dominated by heating from the ground, which results in a temperature decrease with height. Most common atmospheric phenomena, such as clouds, are found here. The troposphere is bound by the tropospause.

The stratosphere starts just after the tropospause and extends to an altitude of about 50 km. In this region the temperature rises with altitude and the primary ozone layer, which absorbs and scatters solar UV radiation, is in this layer. The stratosphere is bound by the stratospause, where the temperature gradient again changes.

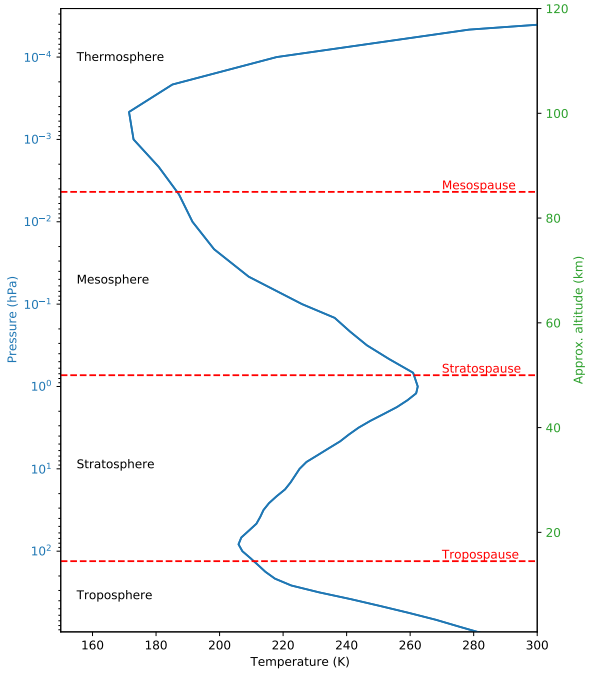

Figure 2.1: Mean vertical temperature profile of the atmosphere in 2020 from MLS V5.0. The five main regions are divided by boundary layers marked by red lines.

The mesosphere reaches from the stratospause to about 85-90 km, and the temperature decreases with height in this region due to radiative cooling by CO_2. The mesosphere holds the D-layer which is the innermost layer of the ionosphere. The D-layer is partly ionized during the day and during solar proton events, ionization in the D-region can reach unusually high levels over high- and polar-latitudes. The mesosphere is bound by the mesospause, which is the coldest region of the atmosphere.

The fourth atmospheric layer is the thermosphere for which the temperature increases with altitude due to high energy UV radiation. The thermosphere has extremely low air density and most of the thermosphere is above the Kárman line (100 km), which by The Fédération Aéronautique Internationale (FAI) is considered outer space. The gases in the thermosphere is not well mixed because of this low density. The remaining ionosphere, namely the E and F-regions, overlaps with the thermosphere. Beyond the thermosphere is the uppermost layer of the atmosphere, the exosphere, which gradually fades into the vacuum of space.

2.1.3 Circulation and auroral heating

The atmosphere is subject to several mass transport processes. The Earth radiate and absorb equal amounts of energy to maintain a constant temperature. The balance between the radiatively driven temperature gradients (i.e. redistribution of thermal energy) and the forcing due to the deposition of gravity wave momentum is the main causes of the large-scale air circulations observed in any region of the atmosphere. The Earth's atmospheric circulation varies from year to year, but the large-scale structure of its circulation remains

fairly constant.

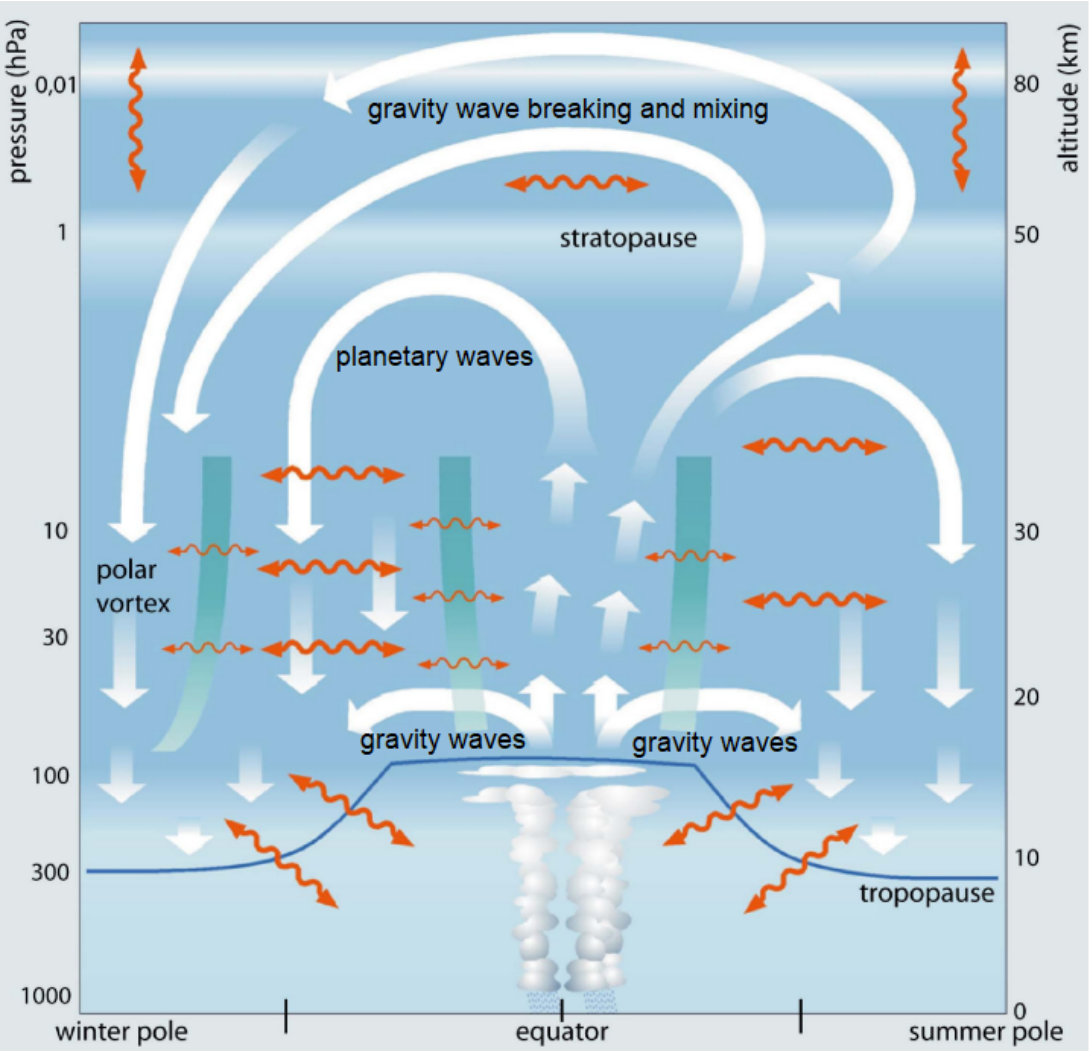

Figure 2.2: Dynamics of the troposphere-stratosphere-mesosphere exchanges including contribution of gravity waves and planetary waves. Thick white arrows represent residual circulation whereas wavy orange arrows indicate two-way mixing processes. Figure adapted from Bönisch et al. (2011).

In the atmosphere radiative temperature gradients in latitudinal direction create latitudinal pressure gradients that drive meridional (N-S) wind. The Coriolis force, which is due to the Earth's rotation, acts perpendicular to the air motion turning the wind zonal (E-W). The balance between the pressure gradient force and the opposite directing Coriolis force is called a geostrophic equilibrium. This gives geostrophic wind that flows along the pressure contours in the atmosphere. In winter the pressure gradient force is towards the cold pole, resulting in an eastward geostrophic flow, and for the summer the pressure gradient force is away from the warm pole giving westward geostrophic wind.

Furthermore, the atmospheric circulation is affected by upward propagating atmospheric waves such as gravity waves, planetary waves and tidal waves. These all carry momentum and energy, and as they propagate upward their amplitude grow exponentially

to compensate for the decrease in atmospheric density. In the stratosphere the vertical wavelength of several waves approaches zero, thus making the wave unstable and depositing its energy and momentum in a thin layer known as a critical level. This momentum deposition by planetary-scale waves gives rise to sudden stratospheric warmings and vortexes in the polar regions.

Planetary-waves that do not reach a critical level continue to propagate upward. At mesospheric altitudes the atmospheric waves eventually break due to an unstable temperature gradient and they affect the global circulation by depositing their energy and momentum. Consequently, wave motions often dominate the wind field in the MLT region. In the winter, with a strong eastward geostrophic flow, the eastward waves all reach critical levels in the stratosphere and only the westward propagating waves continue upward and break. Figure 2.2 show the residual circulation of the troposphere, stratosphere and mesosphere including the contribution of atmospheric waves.

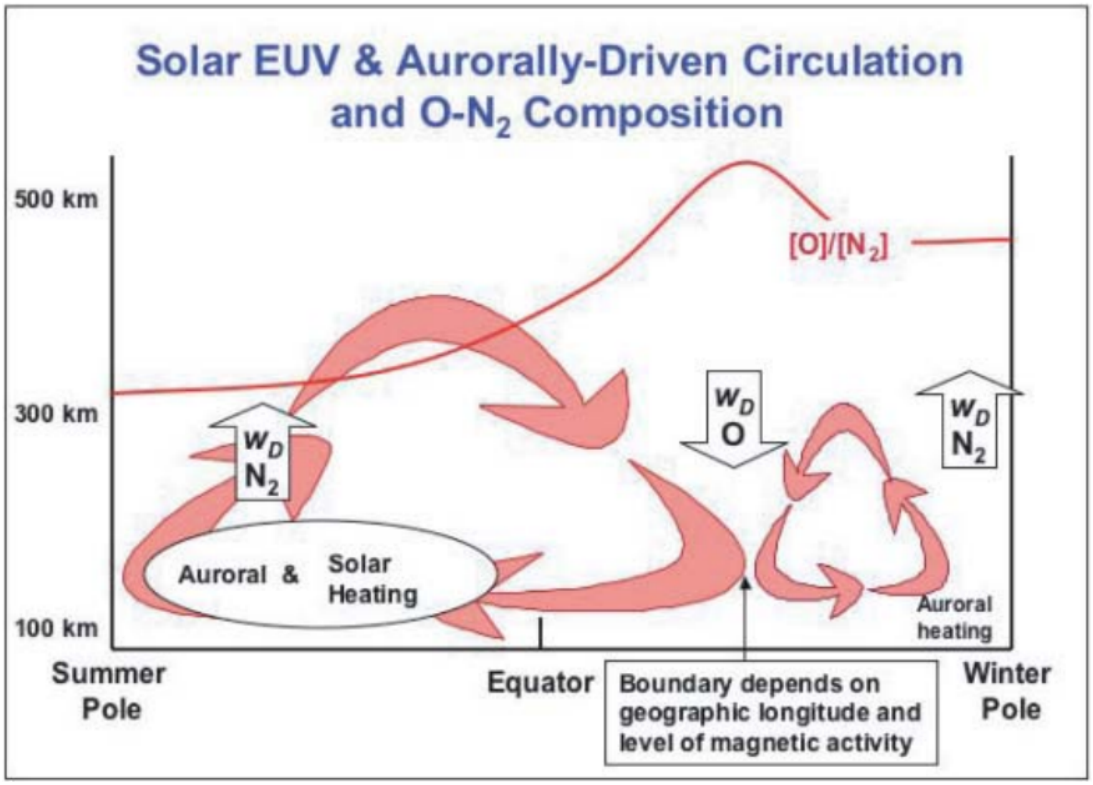

Figure 2.3: Solar EUV and Aurorally-Driven Circulation and O-N_2 Composition of the thermosphere. Illustration borrowed from Forbes (2007).

Figure 2.3 illustrate the circulation processes that take place in the thermosphere. The zonal-mean meridional circulation in the thermosphere is caused by solar heating and transport of O and N_2 through upwelling in the summer hemisphere and downwelling in the winter hemisphere. A weak return flow in the lower thermosphere closes the circulation and maintains continuity of mass flow. A secondary circulation cell appears in the winter hemisphere due to auroral heating at high latitudes. The boundary of the two circulation cells depends on geographic longitude and the level of magnetic activity. The secondary circulation cell can cause a local maximum in the atomic oxygen to nitrogen density ratio [O/N_2] near the boundary of the two cells (Forbes, 2007). The relevance to this thesis is

that atomic oxygen is a source and a sink of ozone.

2.2 The secondary ozone layer

There is a global peak in the ozone abundance known as the secondary ozone layer in the UMLT region of the Earth's atmosphere. Figure 2.4 shows the yearly mean nighttime ozone mixing ratio in 2020 for a vertical axis of both pressure and altitude as a mean of all latitudes. Although the density is lower, the yearly mean nighttime mixing ratio at ~ 95 km is comparable to the stratospheric ozone layer at 30-40 km. Furthermore, a small tertiary ozone layer is located at ~ 75 km. In figure 2.4 the tertiary ozone layer is not clearly visible due to yearly and latitudinal averaging.

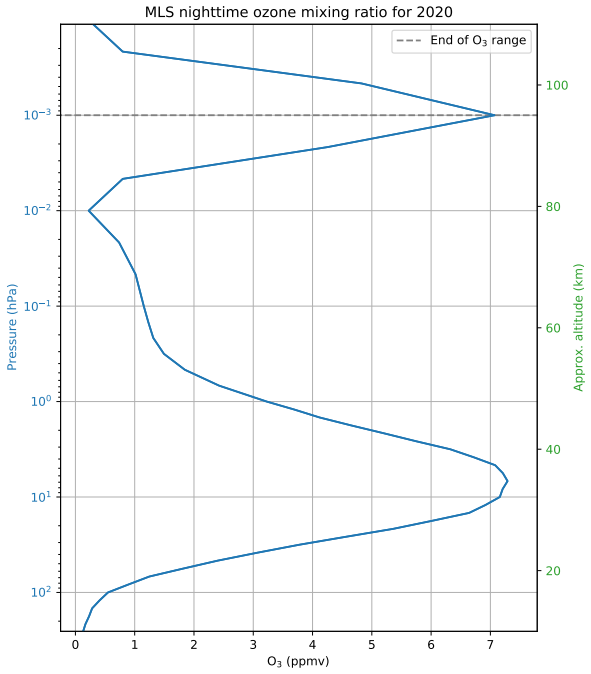

Figure 2.4: Vertical profile of MLS V5.0 nighttime ozone mixing ratio in 2020.

2.2.1 Ozone chemistry

Smith and Marsh described the processes that drive the creation and destruction of mesospheric ozone in 2005 (Smith et al., 2005). There are in total eight kinetic reactions and one photolytic reaction that destroy ozone, while there are only one single production reaction. Mesospheric ozone is created by the reaction

$$O + O_2 + M \rightarrow O_3 + M, \tag{2.1}$$

which is the associative reaction between O and O_2. M indicates the stabilising background species in the atmosphere. Of the in total nine reactions contributing to ozone

destruction, only three reactions play a significant role in the mesosphere. These three reactions are,

$$O_3 + O \rightarrow 2O_2 \tag{2.2a}$$
$$O_3 + H \rightarrow OH + O_2 \tag{2.2b}$$
$$O_3 + h\nu \rightarrow O(1D) + O_2. \tag{2.2c}$$

where O(1D) indicates the excited oxygen atom. Reaction 2.2c gives the photolysis of ozone and this reaction is about an order of magnitude larger than the others. A good approximation when studying ozone loss by kinetic reactions or other sources (such as EPP) is hence to neglect daytime ozone. The two species which significantly destroy nighttime ozone at MLT altitudes are atomic oxygen, O, and atomic hydrogen, H, given by reaction 2.2a and 2.2b, respectively.

A steady-state formula for ozone mixing ratio during night is given by,

$$O_3 = \frac{k_1 \cdot O \cdot O_2 \cdot \rho}{k_2 \cdot O + k_3 \cdot H} \tag{2.3}$$

where ρ is the background number density as defined by the ideal gas law and the the reaction rates are given by,

$$k_1 = 6.0 \times 10^{-24} \left(300/T\right)^{2.4} \tag{2.4a}$$
$$k_2 = 8.0 \times 10^{-12} \exp\left(-2060/T\right) \tag{2.4b}$$
$$k_3 = 1.4 \times 10^{-10} \exp\left(-470/T\right). \tag{2.4c}$$

Reaction rates k_2 and k_3 are proportional to the temperature T, while reaction rate k_1 is inversely proportional (Smith et al., 2005). This indicates that for lower temperature, ozone is created at an higher rate while at the same time being destroyed at a slower rate. This gives higher equilibrium ozone concentrations for decreasing temperature, i.e. a negative theoretical correlation between ozone and temperature at the UMLT region.

2.2.2 CO as a dynamical tracer

In the UMLT region CO has a major source from CO_2 photolysis, described by the chemical reaction,

$$CO_2 + h\nu \rightarrow CO + O. \tag{2.5}$$

The main loss of CO in the lower thermosphere is through the slow recombination reaction with atomic oxygen,

$$CO + O + M \rightarrow CO_2 + M, \tag{2.6}$$

where M indicates the stabilizing background species in the atmosphere.

CO is also produced in the stratosphere by oxidation of atmospheric methane, but it is destroyed through the rapid loss reaction,

$$CO + OH \rightarrow CO_2 + H, \tag{2.7}$$

which is the dominant loss reaction for CO in the stratosphere and mesosphere. Since OH is produced by reactions involving photolysis, its concentration diminished rapidly in the dark. The OH loss reaction therefore only occurs in the daytime atmosphere (Solomon et al., 1985).

Under chemical equilibrium the CO concentration can then be expressed as

$$[CO] = \frac{J\,[CO_2]}{k_4\,[O]\,[M] + k_5\,[OH]}, \tag{2.8}$$

where J is the photo-dissociation rate constant for reaction 2.5 and k_4 and k_5 are the reaction rate constant for reaction 2.6 and 2.7, respectively. Photochemical balance between reaction 2.5 and 2.6 is the main contributor to the CO concentration in the UMLT, making the second denominator term negligible (Lee et al., 2020).

The crossover height of CO nighttime variability by dynamical and chemical influences (~ 75 km) is slightly lower than the height of odd oxygen, making UMLT CO largely under dynamical control (Solomon et al., 1985). This makes nighttime CO a good dynamical tracer in the UMLT.

2.3 Energetic Particle Precipitation

Energetic Particle Precipitation (EPP) refers to highly energetic protons, electrons, neutrons and ions coming from outer space that enter the atmosphere, gets trapped by the Earth's magnetic field and then accelerated into the polar regions of the atmosphere. The particles originate from solar flares or the radiation belts around the Earth and are driven by solar wind conditions and magnetospheric processes. The precipitation particles has a high variation in spatial-, temporal-, flux- and energy-distribution due to the multitude of processes and their dynamical variability.

The particles penetrate deeply into the Earth's atmosphere due to their high energy and velocity, which leads to collisions, ionisation and chemical reactions with atmospheric gases and particles. This is again associated with the creation of NO_X and HO_X which is known to deplete ozone in the primary and tertiary ozone layer (Aikin et al., 1999). From equation 2.3 we know that these gases does not affect the secondary ozone layer, but ozone in this layer can be affected by EPPs in other indirect methods.

There are various types of energetic particles that precipitate into the Earth's atmosphere. Figure 2.5 show different types of EPPs, solar EUV (Extreme ultraviolet) and X-rays involved in atmospheric ionization, well as the ionization altitude profile they create (Mironova et al., 2015). As seen in the figure precipitation from auroral electrons with energies between about 2 to 25 keV occurs down to near 90 km while the precipitation of medium-energy electrons (MEE), such as radiation belt electrons with energies between 30 keV up to a few of MeV penetrate further into the mesosphere.

Solar energetic particles (SEP) are dominated by protons with energies greater than about 10 MeV and are caused by fast, violent energy-burst phenomena on the Sun such as solar proton events, coronal mass ejections and solar flares. The Earth's magnetic field guides

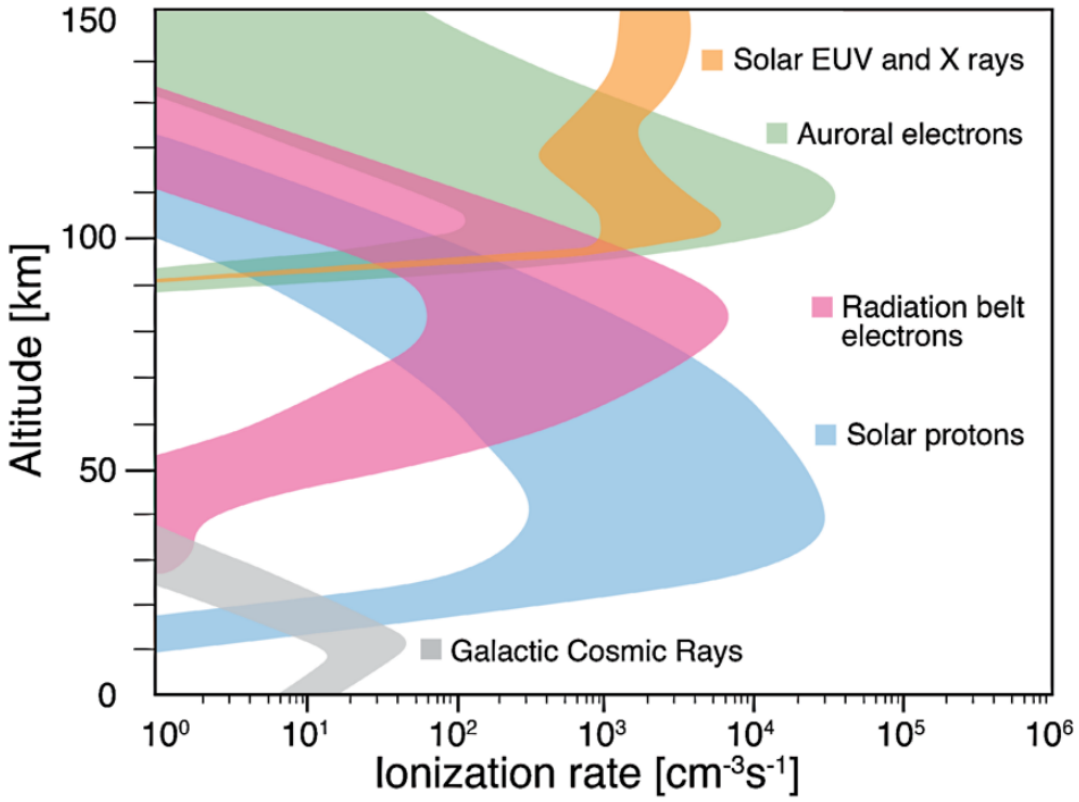

Figure 2.5: Instantaneous ionization rates of EPP, Solar EUV and X rays in Earth's atmosphere. Figure borrowed from Mironova et al. (2015).

the solar protons into the northern and southern polar cap regions ($\leq 60^\circ$ geomagnetic latitude) (Jackman et al., 2006).

2.3.1 Solar Proton Event of 7-10. November 2004

The solar proton event of 7-10. November 2004 is a SPE accompanied by a geomagnetic superstorm. The ionospheric and magnetospheric effects have been studied thoroughly (Panasenko et al., 2007; Rastogi et al., 2012; Simi et al., 2013; Yermolaev et al., 2008). In the mesosphere the effect of the event have been studied in the tertiary layer at 0.02 hPa (77 km) by Hocke (2017) with data from NASA's Microwave Limb Sounder. The study finds strong changes in ozone and temperature in the polar middle atmosphere for the northern winter hemisphere, with the tertiary ozone layer being lost for one week after the event. No study have so far been conducted in the MLT region. The solar proton event is only moderate in perturbation of solar proton flux while its large in perturbed geomagnetic indices, making it a good event to study for correlations between EPP and the secondary ozone layer.

2.3.2 Effect on ozone

EPPs can enhance HO_x (H, OH, HO_2) through the formation of positive ions followed by complex ion chemistry and NO_x (N, NO, NO_2) through the dissociation of molecular nitrogen. At high-altitudes OH and HO_2 concentrations are particularly enhanced by electron deposition, which is correlated with the magnetic index Ap. In the stratospheric (primary) and mesospheric (tertiary) ozone layers the enhancement of these species concentrations are known to deplete ozone (Aikin et al., 1999). In the secondary ozone layer its clear from the chemical equilibrium in equation 2.3 that this layer is not directly affected by HO_x and NO_x from EPP, however the impact of EPP have so far not been fully explored. Idealized simulations by Guttu et al., 2020 using the WACCM model indicate that MEE leads to an ozone depletion of up to 0.15 ppmv or 3.5% in the secondary ozone layer during winter. It is still unclear whether the effect is due to changes in the chemical sources and sinks of secondary ozone or due to indirect effects due to changes in circulation and temperature. The simulations only investigate MEE specifically, while this thesis looks at Ap events. Furthermore, no study on the EPP effect on the secondary ozone layer with satellite data has so far been conducted.

Chapter 3

Instruments

In this chapter the instruments used for collecting data to the thesis are described. Firstly, a description of EOS Aura Microwave Limb Sounder which provides nighttime ozone mixing ratio, temperature and nighttime CO mixing ratio. Then a description of geomagnetic indices, especially the daily Ap index, which has been used for analysing the results.

3.1 EOS Aura Microwave Limb Sounder

The Microwave Limb Sounder is one of the four instruments onboard the Earth Observing System (EOS) satellite Aura, launched by the National Aeronautics and Space Administration (NASA) in July 15 th 2004. Each of the four instruments onboard Aura measure the atmosphere's chemistry and dynamics by detecting the unique spectral signatures of ozone, aerosols and key gases. The goal of these measurements is to gain insight of ozone trends, air quality changes and their linkage to climate change. The MLS measure trace gases in the atmosphere by observing the faint microwave emissions from rotating and vibrating molecules (NASA Goddard, n.d.; NASA Jet Propulstion Laboratory, n.d.). The data set used in this thesis is a gridded version of MLS V5.0 Level 3 data provided by Dong Wu from the MLS team. MLS V5.0 Level 3 ozone data can be accessed here: Schwartz et al. (2021).

Aura was launched into a sun-synchronous near polar (98.2% inclination) orbit, which crosses the equator each day at around 1:30 pm solar time. The satellite is part of the satellite constellation A-train (where 'A' stands for afternoon), and at around 1:30 am the satellite crosses the equator on the night side of the Earth. The orbit is at 705 km above the Earth with a sixteen-day repeat cycle. The MLS observes the thermal microwave emissions from the limb of the atmosphere, and scans the ground up to $\sim$ 100 km every $\sim$25 seconds. The EOS MLS system contains three modules: The GHz radiometer module, the THz radiometer module and the Spectrometer module. MLS Temperature from the stratosphere and above is obtained from bands near O2 spectral lines at 118 GHz, while CO is retrieved from radiance measurements of two bands in the MLS 240 GHz radiometer. The standard product for O3 is obtained from the radiance measurements near 240 GHz.

In January 2022 the newest version of the MLS data set (V5.0) was available to the public. One of the main data processing software updates is an increased vertical range for species such as O3, H2O and CO which has improved the performance retrievals in the upper mesosphere. The new vertical range for O3 is from 261-0.001 hPa, where 0.001 hPa corresponds to $\sim$95 km.

For this thesis, nighttime ozone, temperature and nighttime CO profiles were provided on a longitude-latitude grid for the given pressure profiles. In the data set the longitude grid spans from 176°W-176°E with a 8° interval, while the latitude grid spans from 84°S-84°N with a 4° interval. Each species is provided with nighttime observations with ascending, descending orbits and mean orbit, as explained by the equatorial crossing of the satellite earlier. The nighttime observations are made with a solar zenith angle greater than 100°, ensuring the atmosphere is in darkness from the ground to over 100 km. For nighttime ozone and nighttime CO the descending orbit has been utilized, while temperature readings in this thesis utilize the mean of the descending and ascending orbit. As the Aura MLS was launched in late 2004, this thesis includes measurements from October 2004 - November 2021.

3.2 Geomagnetic indicies

Geomagnetic indices are a measure of geomagnetic activity, which is a signature of the response of the Earth magnetosphere and ionosphere to solar forcing (Menvielle et al., 2010). The indices aim to give a semi-quantitative measure of the level of magnetospheric activity, with each index having different spatial and temporal coverages. The four most commonly used indices are the 'Planetariche Kennziffer' (Kp), the Averaged planetary (Ap), Auroral Electrojet (AE) and Disturbance storm time (Dst) (Rostoker, 1972). In this thesis the Ap index, which is derived from the Kp index, is used to study the auroral particle effect on UMLT ozone.

The Kp index is a three-hour index which was first introduced by J.Bartels in 1949 (Bartels, 1949). The index, ranging from 0 to 9 and given in units of thirds, is derived from the standardized K index (Ks) of 13 magnetic observatories at sub-auroral latitudes. Kp has an quasi-logarithmic scale which does not work well for the calculation of arithmetic means (e.g., daily means, yearly means). Thus, Kp is converted into eight linear ap values, which is the three-hourly equivalent planetary amplitude. The arithmetic mean of the eight ap indices of a UT day rounded to an integer is the daily equivalent planetary amplitude Ap (Matzka, Stolle et al., 2021). The Ap index ranges from 0 to 400, with 0 indicating no geomagnetic disturbance. The daily Ap data in this thesis is provided by the GFZ German Research Centre for Geoscience (Matzka, Bronkalla et al., 2021).

Chapter 4

Analysis

The following chapter explains the method, analysis-steps and models used to obtain the results in the next chapter. Firstly, the steps used to analyse MLS V5.0 and daily Ap indices by themselves is described. Then a comprehensive overview of the comparison between MLS V5.0 and daily Ap indices is provided. This includes the Monte Carlo Bootstrapping significance, the SD-WACCM-X model and the superposed-epoch analysis which all are used to substantiate the relationship between ozone and geomagnetic variability in the secondary ozone layer.

4.1 MLS version 5.0 analysis

The MLS version 5.0 data set has been organised into zonal mean values for nighttime ozone, nighttime CO and temperature at both the 0.002 hPa (∼90 km) and the 0.001 hPa (∼95 km) level. At the 0.002 hPa level, the goal is to compare MLS version 5.0 with the previous MLS version 4.2X by recreating graphs from Lee et al. (2020). This is conducted by analysing the data at three latitude bins (60°S-84°S, 12°S-12°N, 60°N-84°N) and then looking at the climatological variations for each species. Further, the correlation between the species, for given years and highlighted by season, are studied. After comparing the MLS V5.0 to MLS V4.2X at the 0.002 hPa level, the 0.001 hPa level is studied in the same manner.

4.2 Ap index analysis

The Ap indices for all dates present in the MLS version 5.0 data set (October 2004 - November 2021) have been retrieved from the GMZ German Research Centre for Geoscience and merged with the MLS V5.0 data set. Figure 4.1 shows a bin of all Ap indices for the given time-frame, the cumulative Ap distribution and the 95-percentile of the distribution, which in this case is Ap = 24. Throughout this analysis, Ap $\geq$ 24 has been used as the cutoff point for high geomagnetic activity. The background variability is determined by

low Ap, and the low Ap threshold is different depending on the analysis method. For all cases with snapshots in time, the low Ap threshold is Ap $\leq$ 2. This is the 30-percentile of the Ap distribution and is quantitatively giving days of very little geomagnetic activity. For the Superposed Epoch Analysis (SEA), see section 4.3.3, all DJF days with Ap $\leq$ 24 for any of the days in the time composite (day -5 to 10) is used.

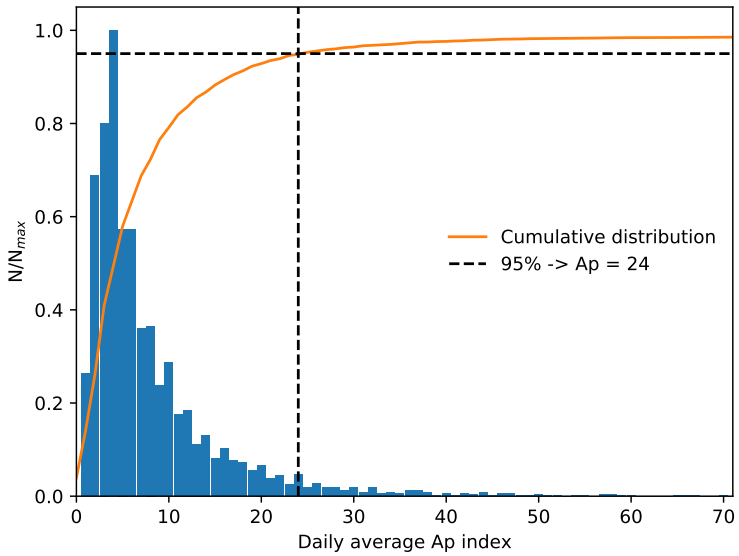

Figure 4.1: Daily average Ap index frequency from October 2004 - November 2021, the cumulative distribution function (orange) and the 95-percentile used at the threshold of a high Ap index values. N is the number of samples in each bin and N_{max} is the highest bin count. The figure is inspired by Lockwood et al. (2018).

Figure 4.2 shows all the daily average Ap indices as a function of time with the high Ap index threshold (black dotted line), the three solar cycles (colored background) and very high Ap index events (Ap $\geq$ 100) marked in red. The figure gives an indication of how many events are considered high Ap events and to see how the Ap index changes with the solar cycles. The red markers has been used to determine a geomagnetic event for a single high Ap case study.

4.3 Comparison of MLS V5.0 and Ap indexes

Throughout this thesis there are several ways that the secondary ozone layer and geomagnetic activity have been compared. Firstly the MLS version 5.0 data has been organized into seasonal zonal-means with high and low Ap values determined by the Ap threshold criteria given in section 4.2. The exact number of high and low Ap cases in each season is found in table 4.1. The differences between the high and low activity days are given in separate plots with the significance of each grid-point given by a 95% confidence interval, described in subsection 4.3.1. Furthermore, the differences between the high and low Ap days in MLS observations are compared with the difference in the velocity streamfunction

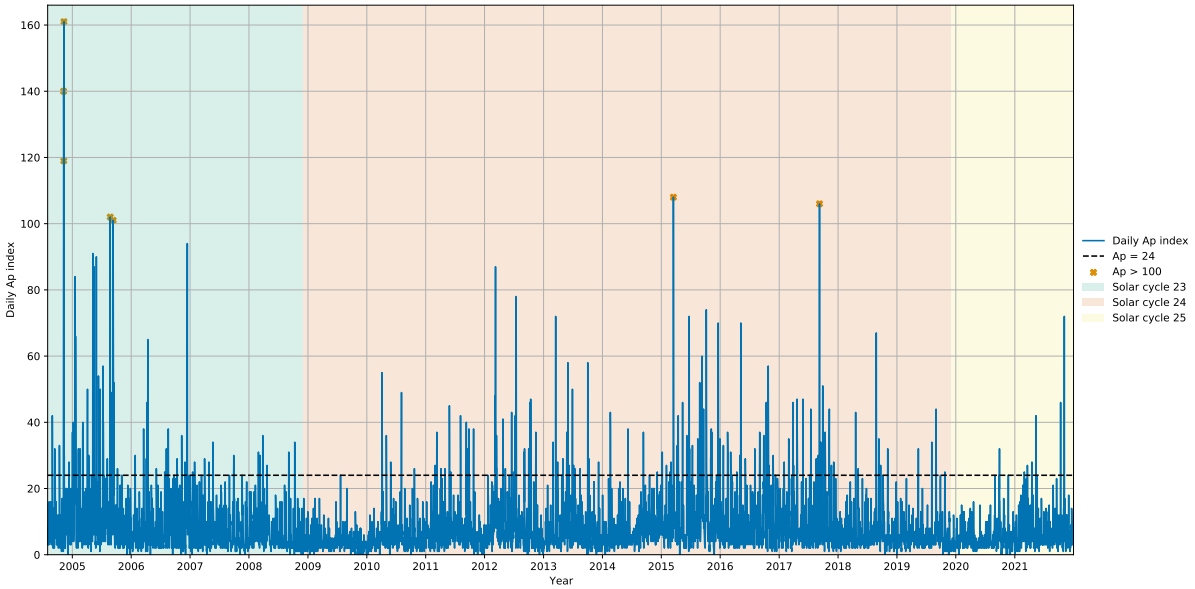

Figure 4.2: All Ap indices (blue) for October 2004 - November 2021 with background colors for solar cycle 23, 24 and 25, a black dotted line for the high Ap threshold and Ap values ≥ 100 marked with a red cross.

given by the WACCM-X model, where the velocity streamfunction has been binned into seasonal high and low Ap days. The WACCM-X model is further described in subsection 4.3.2.

Season	**High Ap**	**Low Ap**
DJF	49	331
MAM	90	171
JJA	63	162
SON	103	313

Table 4.1: Number of high and low Ap cases for each season in seasonal zonal-means.

To further investigate the findings from the seasonal high/low Ap analysis, a single event study of the geomagnetic event 7-10. November 2004 has been carried out. A time series of the geomagnetic variability around the given event is shown in figure 4.3. The solar proton event of 7-10. November is chosen due to it being large in the perturbed geomagnetic indices (Ap = 50 - 160) while having only moderate perturbation in the solar proton flux (Hocke, 2017). Furthermore the event is quiet in geomagnetic variability for the days before and after the event. The event has been analysed in several ways. Firstly the event is analysed by a zonal mean for 5-day bins before, at the event and after which is shown in figure 4.3. Then the difference between these bins is analysed to see how the zonal-mean ozone is changing around the event. Then a time-series for the northern high latitudes (60°N-84°N) at p = 0.001 hPa for MLS nighttime ozone, MLS nighttime CO and MLS temperature over the course of the event has been compared to the MLS climatology with yearly standard deviation from 2005-2020. Additionally, temperature, nighttime ozone and nighttime CO has then been looked as a time-series for all latitudes

at pressure level 0.001 hPa. Lastly the event has been analysed as longitude and latitude maps at pressure level 0.001 hPa for the 5-day bins given in figure 4.3, with the difference between the bins in a separate graph.

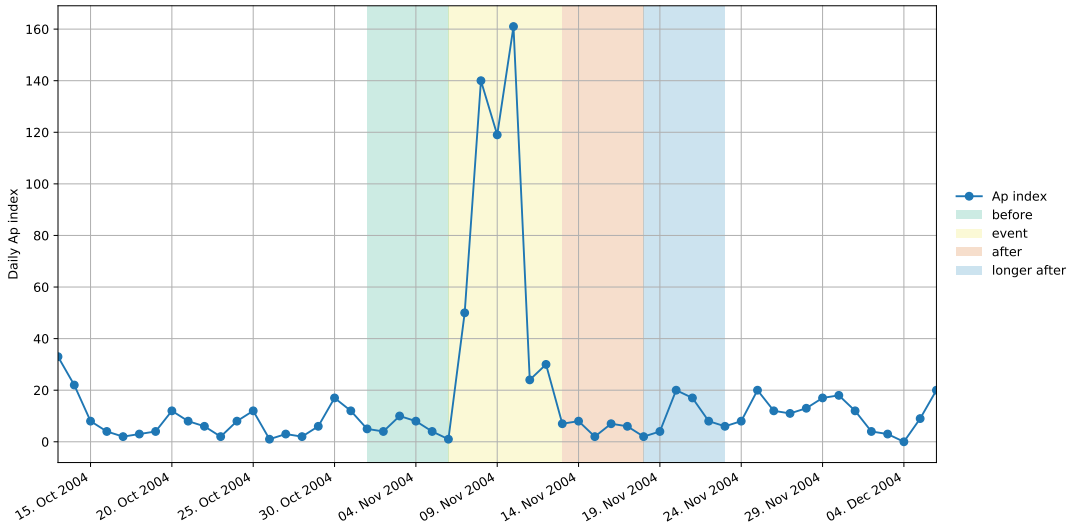

Figure 4.3: Geomagnetic event in November 2004 with colored background for the regions around the event.

To analyse the geomagnetic variability for several different events, a Superposed Epoch Analysis (SEA) has been conducted for the December, January and February season. The superposed epoch has been analysed for all latitudes for nighttime ozone, nighttime CO and temperature. The superposed epoch has been compared with a background atmosphere. A more detailed description of the SEA is found in subsection 4.3.3.

4.3.1 Monte Carlo Bootstrapping significance

Monte Carlo methods, or Monte Carlo simulation, is a collection of computational techniques that relay on repeated random sampling to obtain numerical results. The underlying concept is to use randomness to estimate the possible outcomes of an uncertain event. Bootstrapping, which was first introduced by Efron (1979), is a type of statistical re-sampling applying Monte Carlo methods to observed data. Since its introduction it has become one of the most widely-used statistical methods, and it can be used to determine the sampling distribution of a summary statistic (mean, median, and standard deviation) or a relationship (correlation and regression coefficient) when these are difficult to obtain analytically (Ratick et al., 2009). In this case bootstrapping is used as a basis to calculate statistical significance of both a pressure-latitude grid or a latitude-time grid.

Given a unknown probability distribution, F, a bootstrap sample, x*, is a random sample of size n drawn from F. The bootstrap method used in this thesis obey the following steps (Efron et al., 1995),

(a) Draw $x^{*1}, \ldots, x^{*B}$ independent bootstrap samples from F, where $x^{*b} = (x_1^{*b}, \ldots, x_n^{*b})$ is a vector of n observation which contains the b^{th} bootstrap sample for $b = 1, \ldots, B$.

(b) Evaluate the bootstrap replication corresponding to each bootstrap sample $\Theta^*(b) = T(F(x^{*b}))$ for $b = 1, \ldots, B$, where T is a function.

(c) Compute the uncertainty in Θ from the 95% confidence interval from the histogram. An evaluated value $\Theta = T(F(x))$ is significant if it lies outside the given confidence interval.

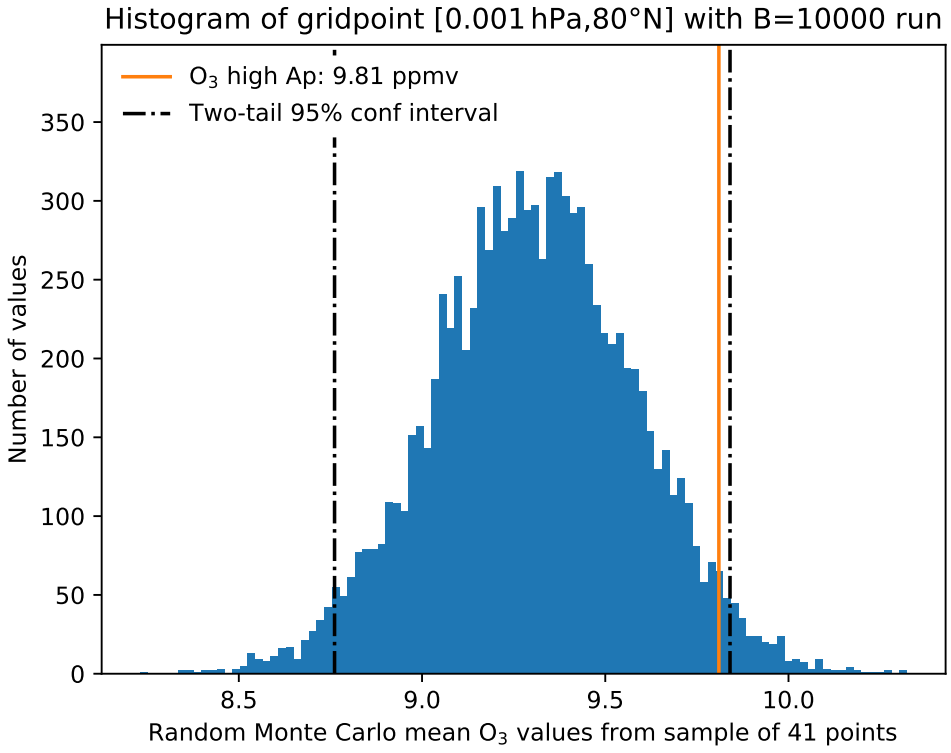

Figure 4.4: Histogram of the Monte Carlo Bootstrapping method at grid-point [0.001 hPa, 80°N] in DJF. Orange line indicates the high Ap O_3 mean, and black stippled line the two-tail 95% confidence interval.

For this thesis the unknown probability distribution F corresponds to all values in a given season, while the random sample size n corresponds to the number of high Ap cases for each season. For each grid-point the method is run B = 10 000 times. Each bootstrap vector of n samples is averaged for the given species giving B = 10 000 mean values. The significance of each grid-point has been calculated from the 95% confidence interval, where significant values are given by the extreme values (i.e. true values outside the 95% confidence interval in a season). The 95% confidence interval is given by two-tails, one at 2.5-percentile and one at 97.5-percentile. Figure 4.4 shows a histogram of grid-point [0.001 hPa, 80°N] in December, January, February (DJF), where the high Ap mean O_3 value is given by an orange line. The given grid-point does not have a significant value for the 95% confidence interval.

4.3.2 The SD-WACCM-X model

In this thesis the NCAR CESM 2.0 extended Whole Atmosphere Community Climate Model (WACCM-X) is used. The Whole Atmosphere Community Climate Model (WACCM) is a comprehensive numerical model which spans from the Earth's surface to the thermosphere (130 km). The model is an inter-divisional collaboration that brings together several aspects of upper atmospheric modeling, middle atmospheric modeling and tropospheric modeling by using the the NCAR Community Earth System Model (CESM) (Baumgaertner et al., 2016) as a numerical framework. The physics of WACCM is described in detail by (Marsh et al., 2013).

In the extended model, WACCM-X, the atmospheric components reach into the troposphere, giving it a top boundary between 500 to 700 km, which is dependent on the solar and geomagnetic variability. The initial release of WACCM-X 1.0 included diffusive processes in the neutral thermosphere and a preliminary implementation of thermospheric neutral dynamics, which is described by Liu et al. (2010). WACCM-X 2.0 further incorporates additional processes such as ionospheric transport, neutral wind dynamo, and calculations of ion/electron energetics and temperatures to correctly resolve the thermospheric energetics and thermal structures. Furthermore the newest release of the model also integrates processes found in the NCAR Thermosphere-Ionosphere-Electrodynamics General Circulation Model (TIE-GCM) (Qian et al., 2014). Thus, WACCM-X 2.0 has the advantage of self-consistently resolving lower atmospheric processes and enable realistic simulation of upper atmospheric variability due to lower atmospheric forcing (Liu et al., 2018).

Hourly output from the specified dynamics configuration of WACCM-X, hereby referred to as SD-WACCM-X, covering the period 2000-2014 was released as part of the National Center for Atmospheric Research (NCAR) Community Earth Model version 2 (CESM 2) and can be accessed through Earth System Grid (https://www.earthsystemgrid.org). The hourly output is archived as daily averaged for this thesis. The model temperature, surface pressure and wind fields are for this configuration constrained below 50 km by NASA Modern-Era Retrospective Analysis for Research and Application (MERRA-2) (Gelaro et al., 2017). In this thesis the wind fields in the atmosphere are described through a velocity streamfunction.

The velocity streamfunction of the residual mean circulation, which is dependent on t, ϕ and z, can be estimated from a latitudinal integration of the vertical component of the residual mean flow ($\overline{\mathrm{w}}^*$) with a boundary condition of Ψ=0 at the North Pole or the South Pole,

$$\Psi\left(t,\phi,z\right) = -\int_{\phi}^{\frac{\pi}{2}} \cos\cos\phi_0 \overline{\mathrm{w}}^* \mathrm{d}\phi_0 \qquad \text{for NH} \tag{4.1a}$$

$$\Psi\left(t,\phi,z\right) = \int_{-\frac{\pi}{2}}^{\phi} \cos\cos\phi_0 \overline{\mathrm{w}}^* \mathrm{d}\phi_0 \qquad \text{for SH} \tag{4.1b}$$

where t,ϕ, z represent time, latitude and altitude and the unit of Ψ is $\mathrm{m\,s^{-1}}$.

For consistency, all daily velocity streamfunction values have been compared to the daily observed geomagnetic Ap index given by GFZ German Research Centre for Geoscience

(Matzka, Stolle et al., 2021). The velocity streamfunction is compartmentalized into average values of high and low Ap indices for each season. The difference in the velocity streamfunction has been compared directly with the difference in MLS V5.0 ozone mixing ratio for the period October 2004 - December 2014. The period is given by the overlapping time for SD-WACCM-X and MLS V5.0.

4.3.3 Superposed Epoch Analysis

The Superposed Epoch Analysis (SEA), also referred to as the composite analysis technique, is a statistical method used in several fields. SEA is used to identify the link between discrete events and spatio-temporal processes and it is useful for isolating low-amplitude signals within data where background variability would obscure detection (Haurwitz et al., 1981). The composite rely on selecting subsets of data which can be identified based on some criteria, such as extreme or unusual events (Laken, B.A. et al., 2013).

In this thesis SEA has been used for a time-series composite around several high Ap events in DJF. High Ap events are chosen by the high Ap threshold (Apgeq24) for day 0. The time-series starts at day -5 and goes to day 10 for all latitudes, making a spatial temporal grid of latitude and time. There are in total 49 high Ap cases for day 0 in DJF, as can be seen from table 4.1. Events missing files for the temporal grid (day -5 to 10) are taken out, leading to a SEA with 41 high Ap events. The background variability is defined as all DJF days without any extreme cases present in the temporal grid, resulting in a background of 887 cases. The MC Bootstrapping method is used on the grid of high Ap cases to determine the significance of each grid-point.

Chapter 5

Results and discussion

The results are divided into several sections. Section 5.1 gives the vertical ozone climatology from MLS V5.0. Section 5.2 directly compares MLS V4.2X and MLS V5.0 at pressure level 0.002 hPa by using and recreating the results from Lee et al. (2020). Section 5.3 focuses on the nighttime ozone climatology at 0.001 hPa, and shows the correlation with CO and temperature at this pressure level. In section 5.4 the analysis of seasonal variability with high and low Ap indexes and the differences between the seasonal means is shown. This includes Monte Carlo significance of the gridded data. Section 5.5 shows a comparison of MLS nighttime ozone high/low Ap difference with the velocity streamfunction from WACCM-X. The results from the case study of 7-10. Nov 2004 are shown in section 5.6, and a superposed epoch of several high Ap events are shown in section 5.7.

5.1 MLS vertical ozone climatological profile

A climatology (2005-2020) of the vertical profile of nighttime ozone for MLS V5.0 is shown in Figure 5.1 for the northern hemisphere, the tropics and the southern hemisphere. Near the mesospause (0.001 hPa) the MLS nighttime ozone display a secondary peak, which for the northern and southern hemisphere is comparable to that of the stratospheric ozone layer ($\sim$ 5-6 ppmv). In the equator the secondary maximum amount is $\sim$ 7 ppmv, while the primary ozone layer displays an amount of $\sim$ 10 ppmv. In the high latitude graphs a tertiary ozone layer is visible at around 74 km ($\sim$ 1 ppmv). From figure 5.1 its clear that the most interesting pressure level when looking for the effect of EPP on the secondary ozone layer is at p = 0.001 hPa.

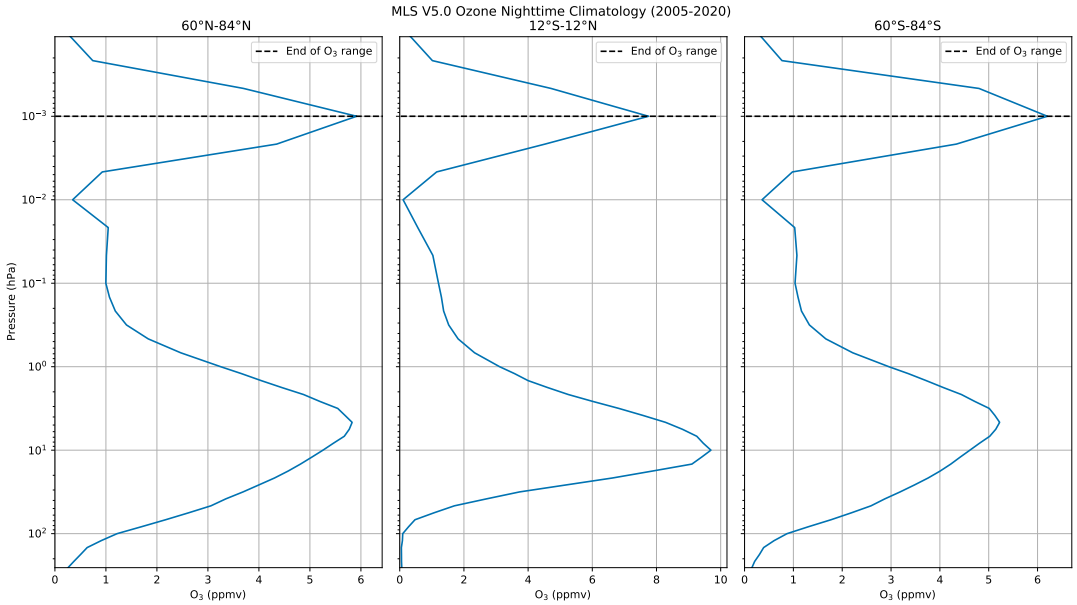

Figure 5.1: Climatology of vertical profiles of MLS V5.0 nighttime O_3 during 2005-2020 at the northern hemisphere (60°N-84°N), the equator (12°S-12°N) and the southern hemisphere (60°S-84°S). A black dotted line indicates the end of the MLS V5.0 ozone range.

5.2 MLS V5.0 compared to MLS V4.2X

In this section MLS V5.0 and MLS V4.2X is compared at pressure level 0.002 hPa by re-creating results from Lee et al. (2020) to confirm the validity and assess the improvements of MLS V5.0. This is important since MLS V5.0 is a new version of the data set which was accessible for the public first in January 2022.

Figure 5.2 shows the climatology of MLS nighttime ozone (blue) and MLS nighttime CO (orange) at 0.002 hPa during the observation period 2005 to 2018 for northern hemisphere high latitudes, southern hemisphere high latitudes and the tropics. Subfigure 5.2a shows the results for the newly released MLS version 5.0 data set, while subfigure 5.2b shows results from MLS version 4.2X. The MLS ozone show the lower part of the maximum ozone layer in the upper mesosphere. For MLS V4.2X the nighttime ozone at 0.002 hPa reaches up to 6 ppmv in high latitudes and 7 ppmv near the tropics, while for MLS V5.0 the nighttime ozone reaches up to 10 ppmv in high latitudes and $\sim$8 ppmv in the tropics. Both versions of the MLS data set shows low amount of ozone ($\leq$2 ppmv) in the local summer season.

In the high-latitude regions, the MLS nighttime ozone display a large annual cycle superimposed on a semiannual cycle, with an early winter maximum and an summer minimum. The northern hemisphere (NH) shows slightly more ozone for the early winter maximum than the southern hemisphere (SH). A semiannual oscillation (SAO) with two seasonal maxima, in early winter and in early spring, is visible for both high latitudes and MLS versions. For MLS version 5.0 the peak in early winter is $\sim$2-3 ppmv higher than in early spring, while for MLS version 4.2X the peak in early winter is only slightly higher than that in early spring. The seasonal variation of nighttime ozone in the tropics shows for

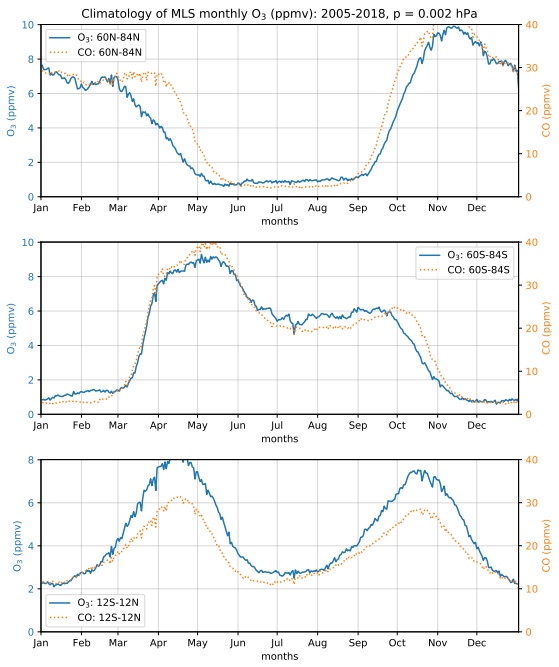

(a) MLS version 5.0

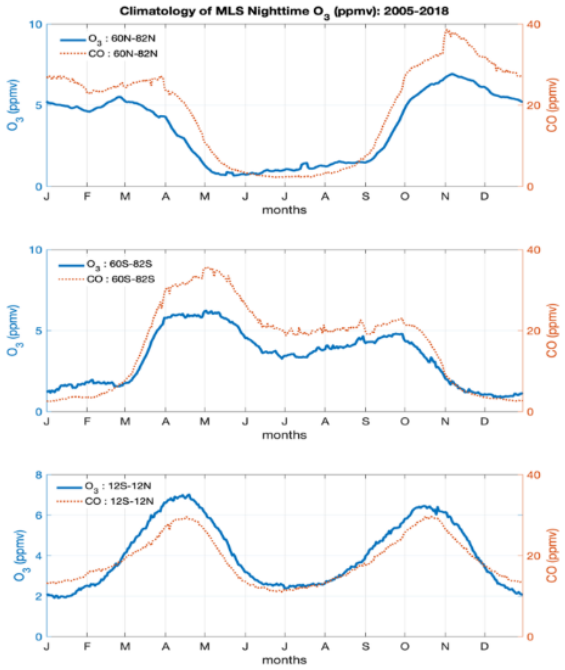

(b) MLS version 4.2X borrowed from Lee et al., 2020

Figure 5.2: Climatology of MLS nighttime ozone (ppmv) at 0.002 hPa during the observation period 2005-2018 for NH high latitude, SH high latitude and tropics from the top. Overlaid orange curves show MLS nighttime CO.

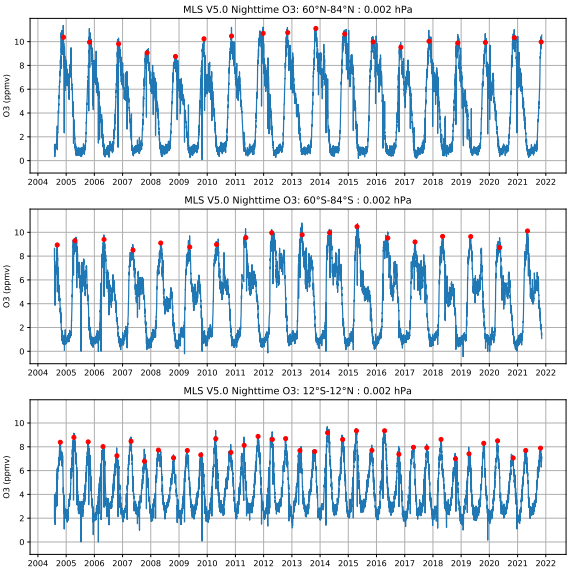

(a) MLS version 5.0

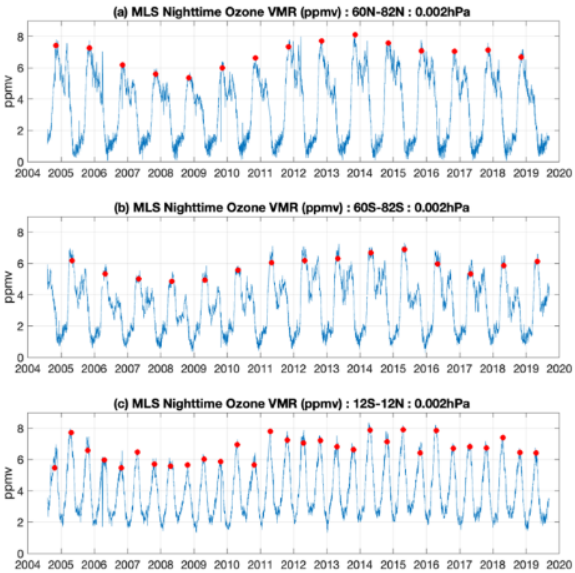

(b) MLS version 4.2X borrowed from Lee et al., 2020

Figure 5.3: MLS daily zonal mean nighttime ozone time-series at 0.002 hPa in NH high latitude, SH high latitude and the tropics for MLS V5.0 and MLS V4.2X. Red markers indicate the annual and semiannual maxima of the O_3 mixing ratios.

both MLS versions an obvious SAO with two equinoctial peaks during April and October. The April peak has slightly more ozone than the October peak, and MLS V5.0 displays more nighttime O_3 for both peaks than MLS V4.2X. Seasonal minima during solstice for both versions show ~ 2 ppmv ozone, similarly to the minima at high latitudes.

The overlaid orange curves in Figure 5.2 denote MLS nighttime CO climatology during the same period. For both versions the seasonal variations of nighttime CO are quite similar to those of nighttime ozone, which indicate similar dynamical and photo-chemical processes associated with atomic oxygen. Details of CO climatology have been described by Lee et al., 2018. In the tropics the seasonal variations in CO display very similar values, while for the high latitude early winter maximum MLS V5.0 display higher nighttime CO values than for MLS V4.2X. Another notable improvement in the MLS V5.0 data set is the smoothing of CO values compared to MLS V4.2X, which clearly is visible in November for the northern hemisphere.

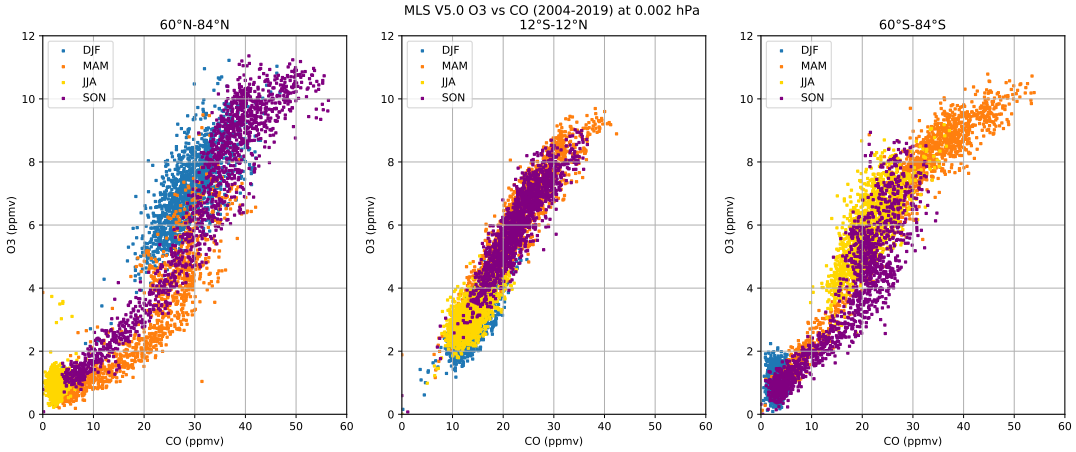

(a) MLS version 5.0

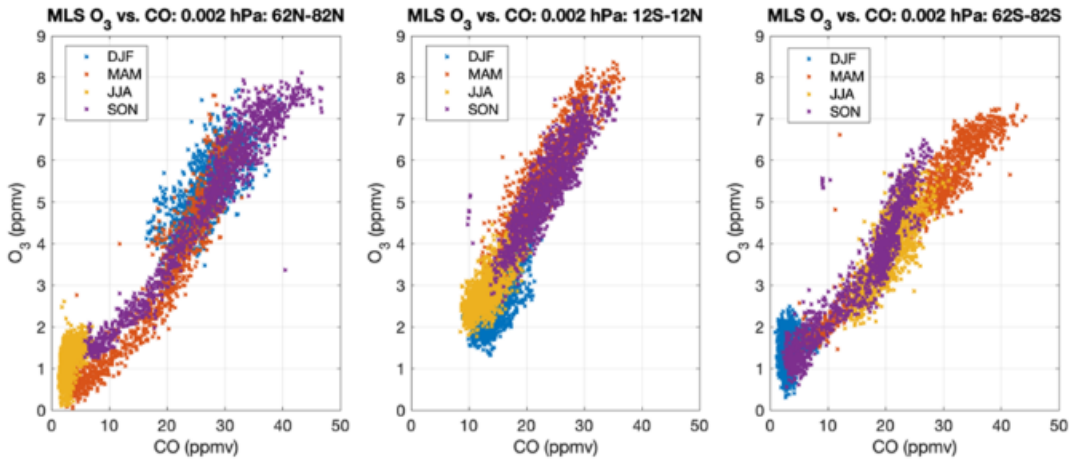

(b) MLS version 4.2X borrowed from Lee et al., 2020.

Figure 5.4: Correlation between daily nighttime O_3 and nighttime CO volume mixing ratios during 2004-2019 at 0.002 hPa for NH high latitudes, tropics as SH high latitudes. The legend indicate the different seasons denoted by colors.

In summary, the ozone distribution between V5.0 and V4.2X are generally very close,

with V5.0 having approximately 20% more O_3 and a slightly larger spring to autumn asymmetry. On the other hand CO from the two data sets are more closely matched in both shape and size.

Figure 5.3 displays the MLS version 5.0 and version 4.2X nighttime zonal mean ozone VMR time series for NH high latitudes, SH high latitudes and the tropics at 0.002 hPa. The SH high latitudes and the NH high latitudes show a similar annual cycle, with an approximately 6-month phase shift between SH and NH. The SAO cycle with two almost equal maxima per year is shown for the ozone time series in the tropics. Along with the annual oscillations, the nighttime ozone time series show a inter-annual variation of ~ 2 ppmv. The inter-annual variation reaches a minimum during 2008-2009, a maximum during 2013-2014 and a new minimum around 2017-2019, which is due to the 11-year solar cycle modulation.

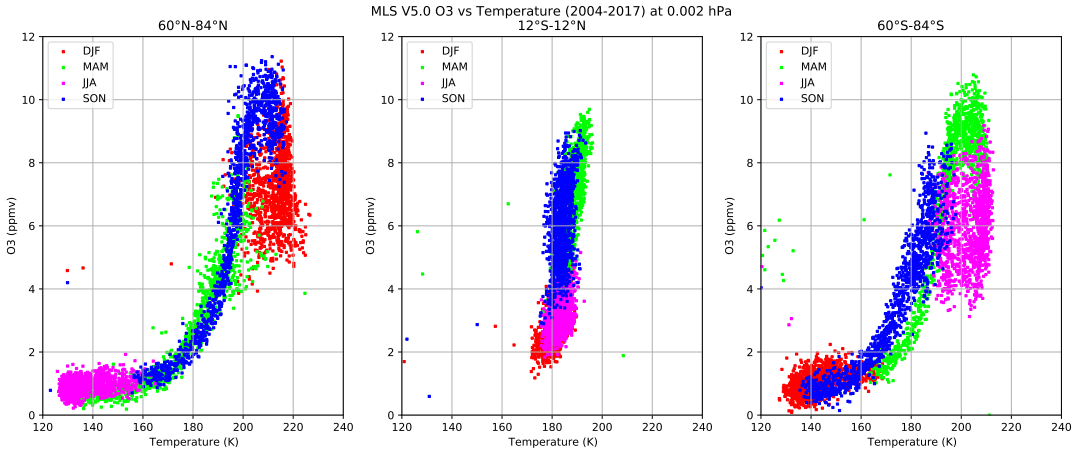

(a) MLS version 5.0

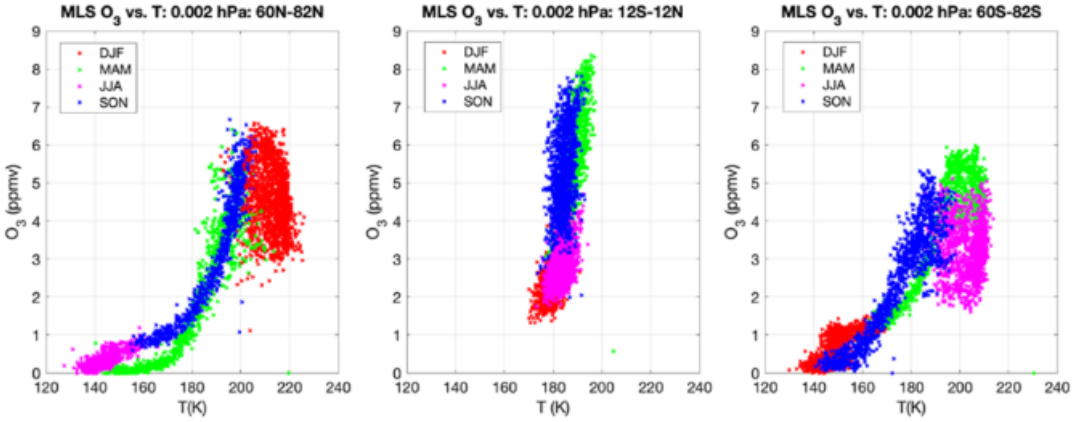

(b) MLS version 4.2X borrowed from Lee et al., 2020.

Figure 5.5: Correlation between daily nighttime O_3 volume mixing ratio and temperature during 2004-2017 at 0.002 hPa for NH high latitudes, tropics and SH high latitudes. The legend indicate the different seasons denoted by colors.

Figure 5.4 shows a strong correlation between nighttime ozone and CO volume mixing ratios (VMRs) for all latitudes. This confirms the dynamical modulation of nighttime ozone in the UMLT region. For high latitudes, the correlation is nearly zero in the

summer season (June, July, August for NH and December, January, February for SH) due to very low concentrations of ozone.

MLS V4.2X and MLS V5.0 show the same trends for the correlation between nighttime ozone VMR and nighttime CO VMR. For MLS V5.0 both ozone and CO indicate higher values than for MLS 4.2X, which is to be expected from the findings in figure 5.2 and figure 5.3. A notable difference is that the ozone volume mixing ratio reaches higher values for the high latitudes than for the tropics for MLS V5.0, which is not the case for MLS 4.2X where the tropics reach higher than the high latitudes.

Figure 5.5 examine the temperature dependence of MLS nighttime ozone at 0.002 hPa and compares MLS V5.0 and MLS V4.2X. The temperature dependence is not solely positive or negative, but changes with location and season. This indicates a complex role of temperature in ozone chemistry and the mesospheric dynamics. For example, in polar regions descending air increases the O_3 mixing ratio, but also causes adiabatic heating that can reduce levels. For most seasons and latitude bins the temperature dependence is positive, except during NH high latitudes during winter (DJF). During fall (SON) for all temperature bins the temperature and nighttime ozone dependence is strongly positive.

In summary, the correlation between nighttime O_3 and nighttime CO is strictly positive for all seasons and follows the same trends for V5.0 and V4.2X, with approximately 25% more O_3 for V5.0. The correlation between ozone and temperature is complex, with both positive and negative correlations, but show similar trends in MLS V5.0 and V4.2X.

5.3 Ozone climatology and correlation at 0.001 hPa

To show the variability of O_3 with EPP effects, it is important to quantify the natural variations due to season, temperature and dynamical effects. This section shows the results for the MLS V5.0 climatology and species correlation at pressure level 0.001 hPa, which is the secondary ozone maximum for MLS V5.0 as seen in earlier figure 5.1.

Figure 5.6 shows the 2005-2020 climatology for MLS V5.0 nighttime ozone for northern high latitudes (60°N-84°N), southern high latitudes (60°S-84°S) and the tropics (12°S-12°N), where MLS nighttime CO has been included in subfigure 5.6a and MLS temperature has been included in subfigure 5.6b.

In the northern hemisphere (60°N-84°N) the ozone layer reaches up to 12.5 ppmv in November and shows a large annual cycle imposed on a semiannual cycle. The southern hemisphere (60°S-84°S) shows a similar cycle, with values slightly lower than the NH. In both cases, the MLS nighttime O_3 climatology shows a semiannual oscillation (SAO) with two seasonal maxima. The maximum values are in early winter (Oct/Nov in NH and Apr/May in SH) and in early spring (Feb/Mar in NH and Aug/Sept in SH), with the peak in early winter slightly higher than the one in early spring. In the tropics the seasonal variation of nighttime ozone show an obvious SAO with maximum peaks of ozone reaching ~ 12 ppmv in mid April and mid October. For the high latitudes seasonal minima show ~ 2 ppmv, while for the tropics the seasonal minima show ~ 4.5 ppmv.

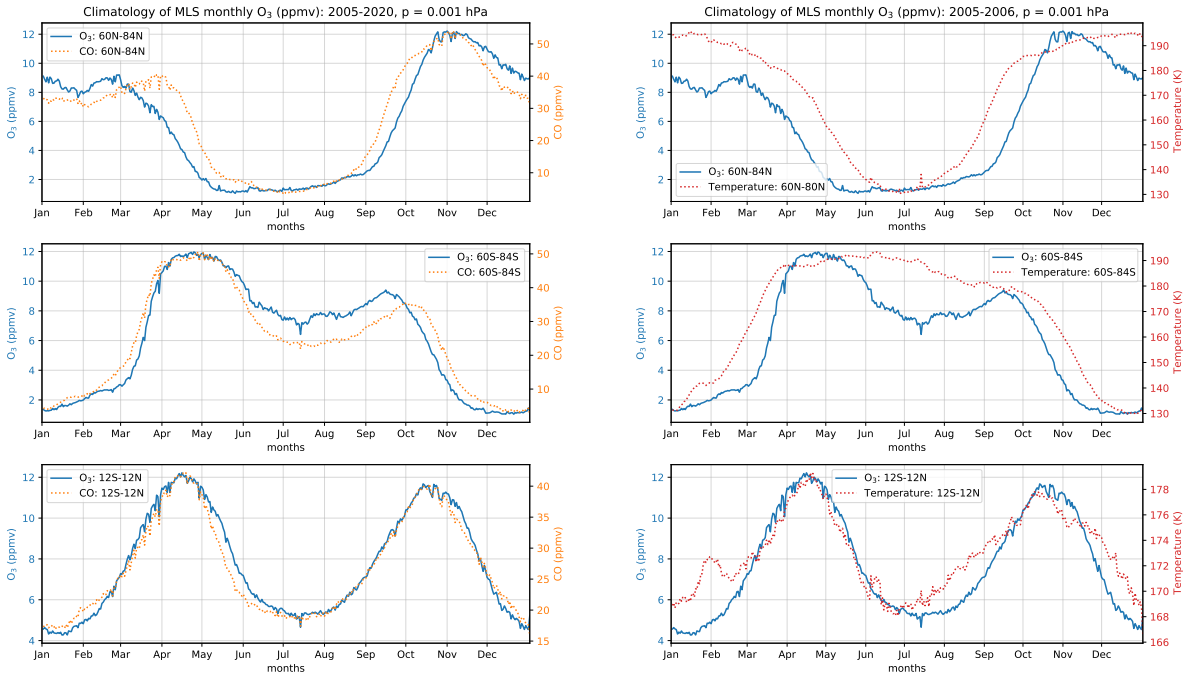

(a) Ozone and CO

(b) Ozone and Temperature

Figure 5.6: Climatology of MLS nighttime ozone (ppmv) at 0.001 hPa during the observation period 2005-2020 for NH high latitude, SH high latitude and tropics from the top. Overlaid orange curves in subfigure 5.6a show MLS nighttime CO and overlaid red curves in subfigure 5.6b show MLS temperature.

The seasonal variations shown in MLS nighttime ozone at 0.001 hPa are similar to that of 0.002 hPa. In general the maxima values in 0.001 hPa are higher than they were for 0.002 hPa, and in high latitudes the early spring maxima is more defined for 0.001 hPa. The MLS nighttime CO clearly have similar dynamics as MLS nighttime ozone. MLS temperature show a SAO with two clear peaks corresponding to the MLS nighttime ozone in the tropics and a small unknown peak in February. In high latitudes the temperature in this pressure level is at its highest (∼180-190 K) during the late autumn, winter and early spring. In summer (JJA for NH and DJF for SH) the temperature drops to about ∼130 K for high latitudes. In general, the temperature is complicated in regions where adiabatic ascent or descent takes place.

Figure 5.7 show the correlation between MLS nighttime O_3 and MLS nighttime CO at 0.001 hPa. The correlation is slightly more spread out than for 0.002 hPa, but still shows a strong positive correlation which confirms the dynamical modulation of nighttime ozone in the UMLT region.

The correlation between MLS nighttime ozone and MLS temperature at 0.001 hPa is shown in figure 5.8. As for 0.002 hPa, the correlation at 0.001 hPa is not solely positive or negative which indicates the complex chemistry and dynamics of ozone's dependence on temperature. At high latitudes during winter (DJF for NH and JJA for SH) the correlation is slightly negative, while for most seasons and latitude bins the correlation is positive. The daily MLS nighttime ozone reaches up to 14 ppmv for all latitude bins, which

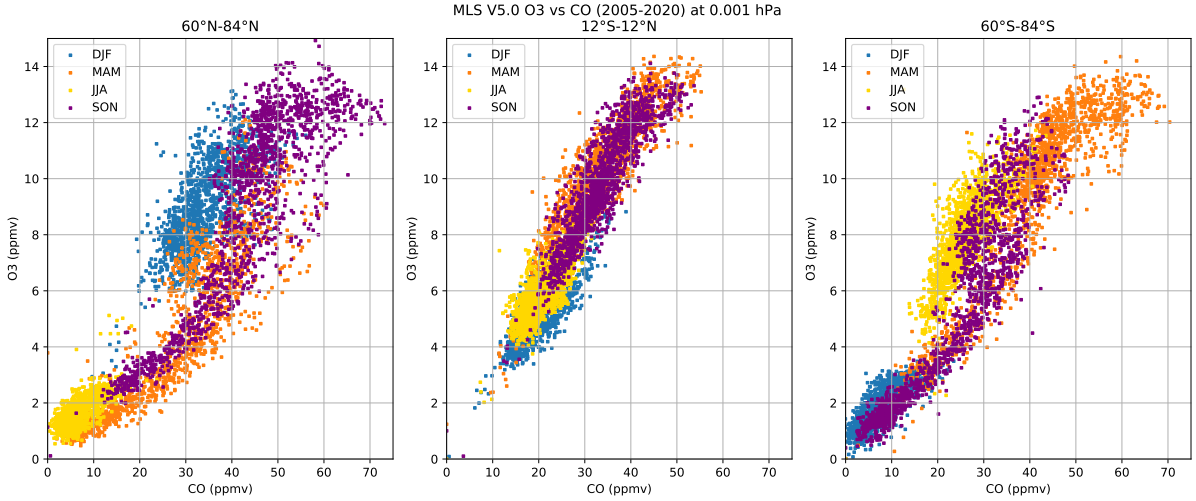

Figure 5.7: Correlation between MLS daily nighttime ozone and nighttime CO during 2005–2020 at 0.001 hPa for northern high latitudes (60°N–82°N), tropics (12°S–12°N), and southern high latitudes (60°S–82°S). Colors denote different seasons as indicated by the legend.

is higher than for 0.002 hPa. The rapid correlation in the summer to winter transitional seasons, MAM and SON, makes these seasons harder to interpret when looking for effects of EPP on ozone mixing ratios at this pressure level.

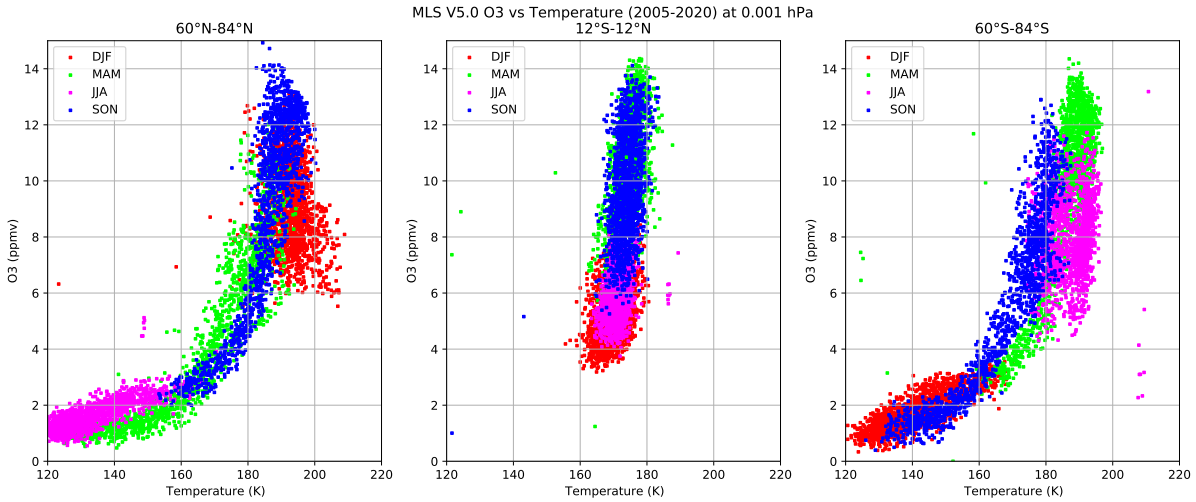

Figure 5.8: Correlation between MLS daily nighttime ozone and temperature during 2005–2020 at 0.001 hPa for northern high latitudes (60°N–82°N), tropics (12°S–12°N), and southern high latitudes (60°S–82°S). Colors denote different seasons as indicated by the legend.

In summary, MLS V5.0 give about 20% higher O_3 values for pressure level 0.001 hPa than 0.002 hPa, with both pressure levels showing similar trends for the natural variations due to season, temperature and dynamical effects. At 0.001 hPa the secondary peak at high latitudes is even clearer than for 0.002 hPa. When further analysing the effects of EPP on nighttime ozone its clear that the most interesting regions of ozone is at high latitudes

is the winter season (DJF in NH and JJA in SH). The spring and autumn season is heavily affected by dynamics in the atmosphere. The effect with temperature is hard to interpret as, but the negative and positive correlation between ozone and temperature at high latitudes in DJF and JJA respectively is of great interest for further analysis in this thesis.

5.4 Seasonal geomagnetic variability in ozone

In order to determine the effect of EPP on the secondary ozone, I have separated the seasonal zonal-means of MLS V5.0 nighttime ozone into high and low Ap populations. For each season the latitudinal cross sections for $\mathrm{Ap} \geq 24$ and $\mathrm{Ap} \leq 2$ and the difference plot, including markings for the significant grid-points, is discussed.

Seasonal means for DJF and JJA

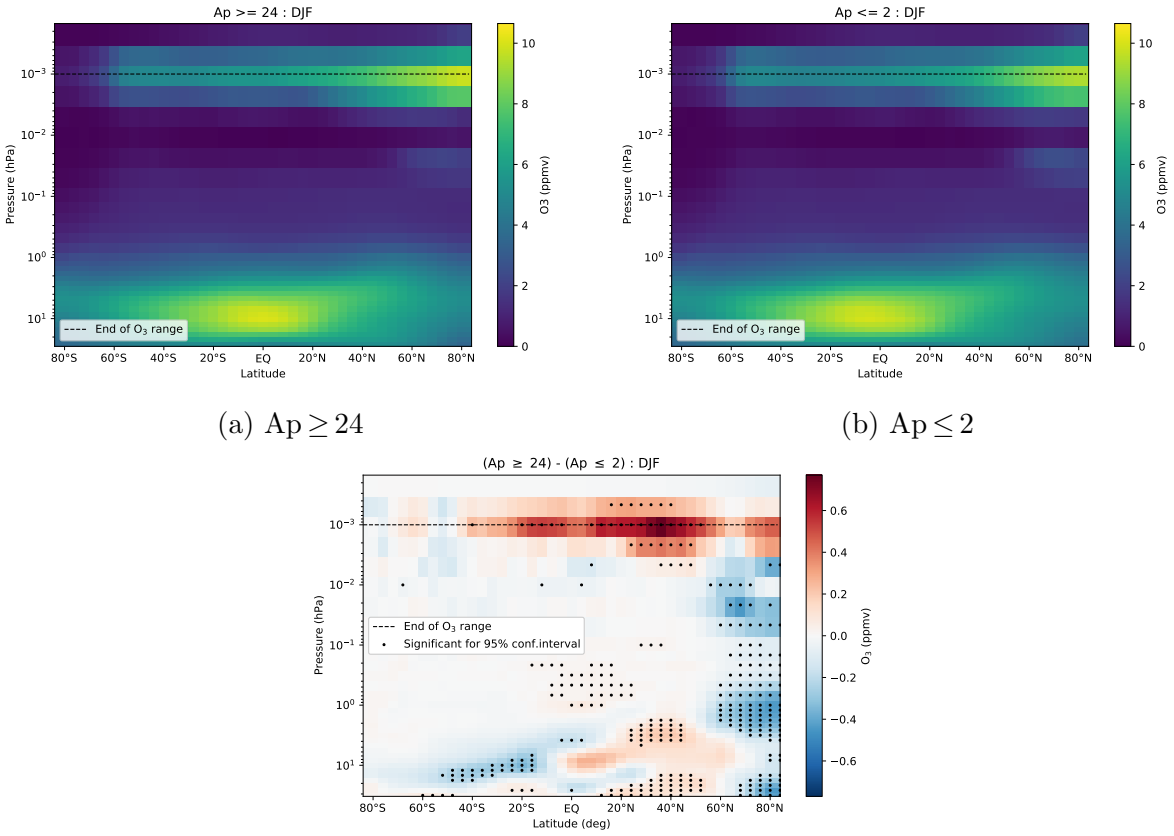

(a) $\mathrm{Ap} \geq 24$

(b) $\mathrm{Ap} \leq 2$

(c) $\mathrm{Ap} \geq 24$ - $\mathrm{Ap} \leq 2$.

Figure 5.9: The mean O_3 mixing ratio (ppmv) cross-sections of high Ap, low Ap and the difference between high and low Ap for December, January and February (DJF) from 2004-2021 as function of pressure and latitude. Significant values by the 95% level for MC-method is marked by black dots.

The December, January, February (DJF) and June, July, August (JJA) ozone mixing ratio during high and low geomagnetic activity as well as their differences (High-Low Ap) and statistical significance of those differences, are shown in figures 5.9 and 5.10 respectively. Both DJF and JJA show an significant ozone depletion for high latitudes in the winter hemisphere (NH for DJF and SH for JJA) in the primary and tertiary ozone layers, as well as an enhancement in low latitudes for the stratosphere. These ozone depletion processes are linked to ozone-depleting catalytic substances, such as nitric oxides, and are to be expected from previous research on the primary and tertiary ozone layer.

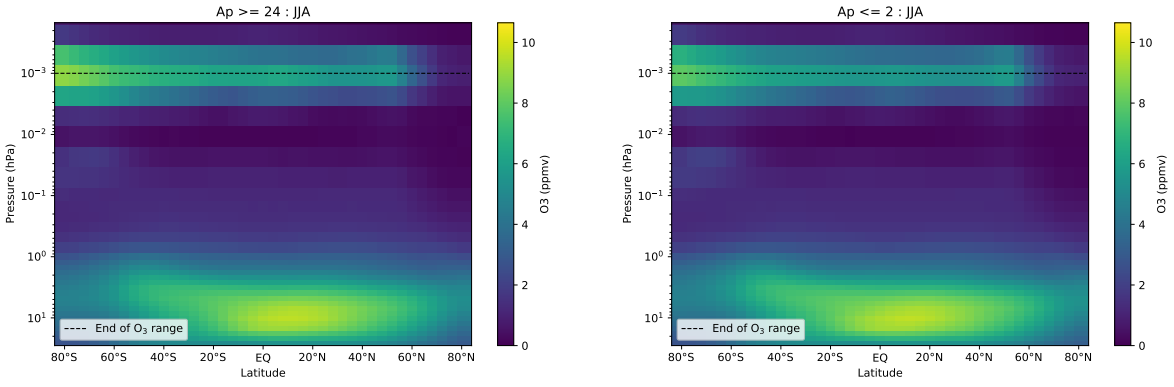

(a) $Ap \geq 24$

(b) $Ap \leq 2$

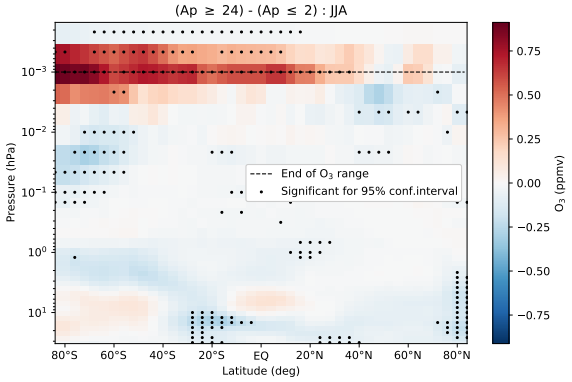

(c) $Ap \geq 24$ - $Ap \leq 2$

Figure 5.10: The mean O_3 mixing ratio (ppmv) cross-sections of high Ap, low Ap and the difference between high and low Ap for June, July and August (JJA) from 2004-2021 as function of pressure and latitude.Significant values by the 95% level for MC-method is marked by black dots.

In the UMLT at pressure level 0.001 hPa the figures show an enhancement in ozone abundance. The enhancement starts at high winter latitudes and expands to lower latitudes.

For the southern high latitudes in JJA the ozone enhancement is considered significant at the 95% level as determined by the Monte Carlo method, while for northern high latitudes in DJF there is an enhancement but it is not of a significant value. This increase in ozone mixing ratio could originate in the auroral heating above, and the induced meridional circulation (Forbes, 2007) in the atmosphere, which would increase the amount of atomic oxygen, decrease the temperature and thus increase the amount of ozone at these levels.

Seasonal means for MAM and SON

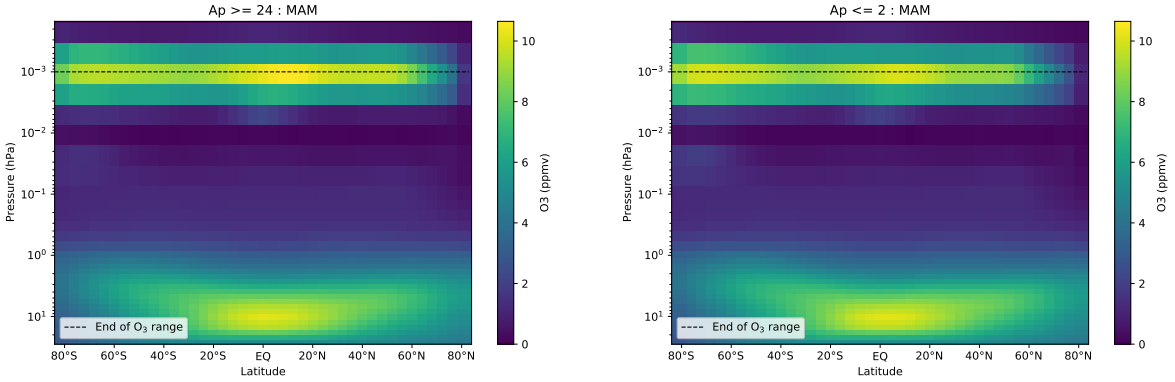

(a) Ap $\geq$ 24 (b) Ap $\leq$ 2

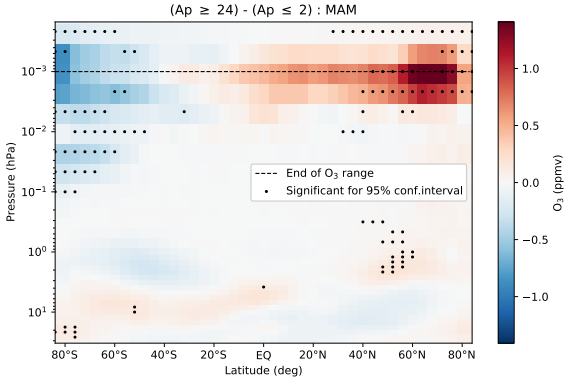

(c) Ap $\geq$ 24 - Ap $\leq$ 2

Figure 5.11: The mean O_3 mixing ratio (ppmv) cross-sections of high Ap, low Ap and the difference between high and low Ap for March, April and May (MAM) from 2004-2021 as function of pressure and latitude.Significant values by the 95% level for MC-method is marked by black dots.

Ozone mixing ratios for high Ap, low Ap and the difference (high-low Ap) in March, April, May and September, October, November are shown in figured 5.11 and 5.12. The MAM and SON seasons are transitional seasons where the sunlit regions moves from high latitudes in one hemisphere to high latitudes in the other hemisphere, as seen in previous figure 5.6 on the ozone climatology. Both MAM and SON show ozone depletion at high latitudes in the secondary and tertiary layers, where the depletion is in the SH for MAM and in the NH for SON. At southern high latitudes in April and May the climatological variability in O_3 has already reached high O_3 values, and thus the significant depletion shown in figure 5.11 is due to EPP effects. The same holds for the significant ozone depletion at northern high latitudes in figure 5.12, where for October and November have high nighttime ozone and the depletion is because of EPP effects. In the opposite high latitudes (NH for MAM and SH for SON), there is a ozone enhancement which extends towards lower latitudes and the tropics, which also has significant values in the secondary ozone layer. For the regions of ozone enhancement there is only one month that show high ozone values for the climatological variability (March for NH and September for SH). The ozone enhancement at high northern latitudes in MAM, which most likely originates from

high Ap events in March, corresponds with the ozone enhancement seen in DJF. The same holds for the ozone enhancement shown in JJA and SON (originating from September events). As for DJF and JJA, the increase in ozone mixing ratio could originate in the auroral heating above, and the induced meridional circulation.

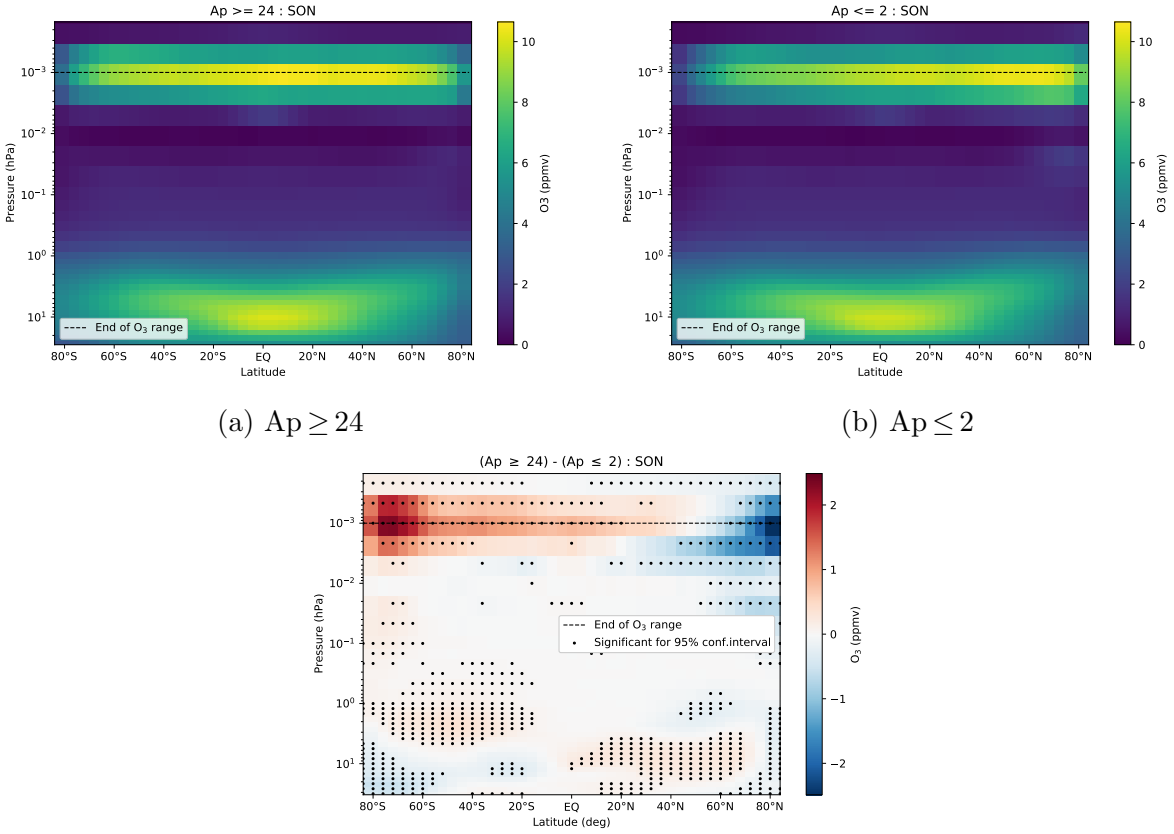

(a) Ap $\geq$ 24

(b) Ap $\leq$ 2

(c) Ap $\geq$ 24 - Ap $\leq$ 2

Figure 5.12: The mean O_3 mixing ratio (ppmv) cross-sections of high Ap, low Ap and the difference between high and low Ap for September, October and November (SON) from 2004-2021 as function of pressure and latitude.Significant values by the 95% level for MC-method is marked by black dots.

In summary, the seasonal zonal-means of MLS V5.0 nighttime ozone show an significant enhancement in ozone at high latitudes in winter seasons (DJF for NH and JJA for SH), which also is visible in the early spring season (March for NH and September for SH). This increase could originate in the auroral heating above and the induced meridional circulation. In the mid to late autumn seasons (October, November for NH and April, March for SH) there is an ozone depletion in the secondary ozone layer which corresponds to simulation results from Guttu et al. (2020). Results from Guttu et al. (2020) is not directly comparable as they investigated MEE specifically, while this study look at Ap events.

5.5 SD-WACCM-X residual circulation

To examine the effects of EPP on the circulation and thus ozone, the residual (transport) circulation given by the velocity streamfunction from SD-WACCM-X is compartmentalized into seasonal zonal-means of high and low Ap indices. The difference in high and low velocity streamfunction is compared with the MLS V5.0 ozone mixing ratio difference between high and low Ap for years 2004 - 2014.

Velocity streamfunction for DJF and JJA

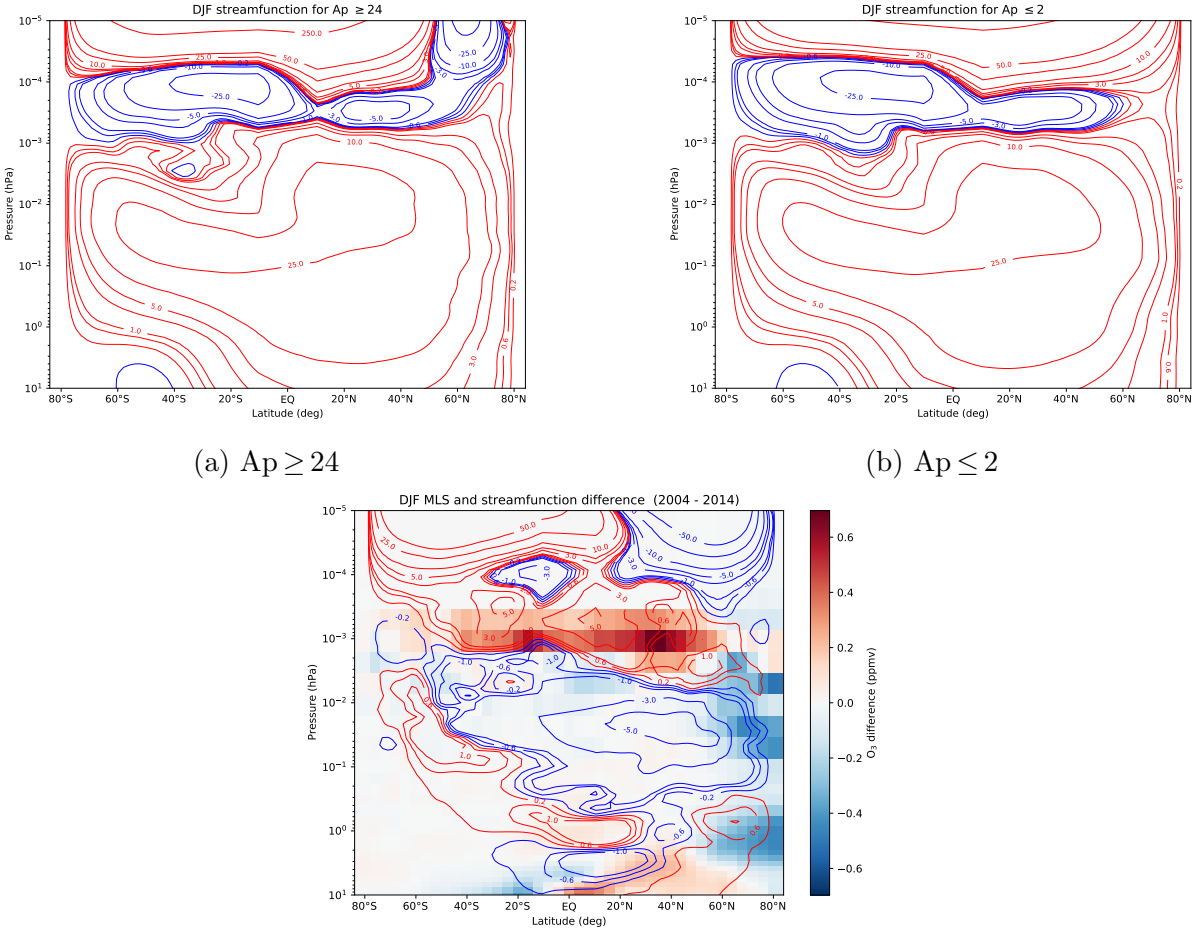

(a) Ap ≥ 24

(b) Ap ≤ 2

(c) Ap ≥ 24 - Ap ≤ 2

Figure 5.13: Velocity streamfunction from SD-WACCM-X for high and low Ap values in December, January and February (DJF) where red indicates clockwise circulation and blue indicated anti-clockwise circulation. Subfigure 5.13c shows the change in velocity streamfunction (high-low Ap) and the MLS ozone mixing ratio difference for years 2004-2014.

Figure 5.13 and 5.14 show the velocity streamfunction given by SD-WACCM-X for high and low geomagnetic activity for December, January, February (DJF) and June, July and August (JJA) respectively. Red streamlines indicate an clockwise circulation in the

atmosphere, and blue streamlines indicate an anti-clockwise circulation. The difference in the high and low geomagnetic activity in the velocity streamfunction is compared to the difference in the MLS ozone mixing ratio in subfigures 5.13c and 5.14c for DJF and JJA respectively. For these subfigures the red streamlines indicate a net increase in the circulation, and the blue streamlines indicate a net slowdown of the circulation because of high Ap.

DJF generally shows a clockwise circulation for the atmosphere up to 0.001 hPa. In the UMLT (10^{-3} - 5×10^{-4} hPa) a anti-clockwise circulation is apparent for DJF. Above this region the circulation matches that of the lower atmosphere with clockwise circulation for DJF. For the velocity streamfunction at high Ap days the UMLT circulation extends up in the NH for DJF, when compared to the circulation of low Ap days. Hence, high Ap influences the transport and circulation into mid and low latitudes for DJF as it interacts with the lower thermospheric circulation (anti-clockwise cell at 10^{-3} - 5×10^{-4} hPa).

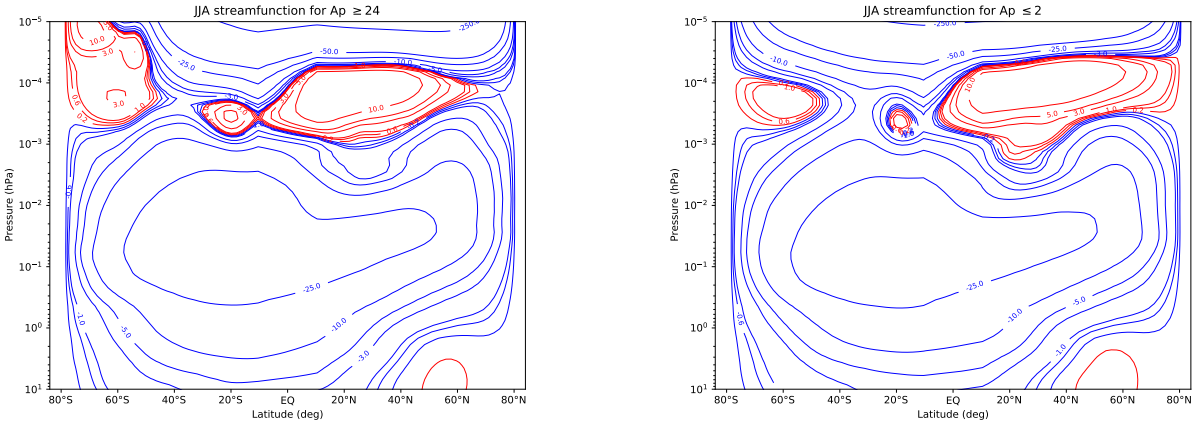

(a) Ap ≥ 24 (b) Ap ≤ 2

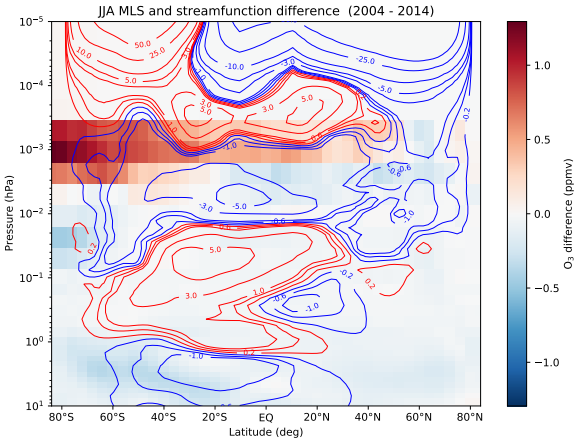

(c) Ap ≥ 24 - Ap ≤ 2

Figure 5.14: Velocity streamfunction from SD-WACCM-X for high and low Ap values in June, July, August (JJA) where red indicates clockwise circulation and blue indicated anti-clockwise circulation. Subfigure 5.13c shows the change in velocity streamfunction (high-low Ap) and the MLS ozone mixing ratio difference for years 2004-2014.

In the UMLT at around 0.001 hPa the DJF difference shows a speed-up of the circulation

due to high Ap at the ozone enhancement at mid latitudes. A blue slowdown in circulation from the thermosphere is located at northern latitudes. At around 20-60°N the relative downwelling from the circulation cells results in higher temperatures and higher ozone, as seen for the tropics in the slightly positive correlation from DJF in figure 5.8. For the southern hemisphere there is an relative upwelling at high latitudes, which according to the correlation at these latitudes causes less ozone. The ozone in the southern hemisphere is also heavily affected by the sun. In northern high latitudes for DJF, the ozone-temperature correlation is slightly negative. This means that for latitudes around 60-84°N the higher temperature from the blue cell will cause decrease in ozone.

JJA displays an anti-clockwise circulation in the atmosphere up to 0.001 hPa. In the UMLT (10^{-3} - 5×10^{-4} hPa) a clockwise circulation is apparent for JJA. For JJA, high Ap interacts with the lower thermospheric circulation at high southern latitudes in the red anomaly (clockwise cell at 10^{-3} - $5{\times}10^{-4}$ hPa). This circulation cell is broken by a anti-clockwise circulation which affects both lower and higher altitudes. In northern latitudes the downward motions from low Ap are suppressed at high Ap circulation (i.e. compression of red clockwise cell between 10^{-3} - $5{\times}10^{-4}$ hPa).

The ozone and temperature in JJA is strictly positive correlated for all latitudes, as shown in figure 5.8. For the circulation in subfigure 5.14c, this means that the relative downwelling, which causes higher temperatures, gives higher ozone and the relative upwelling drives lower ozone. For the northern high latitudes (60-84°N) there is an relative upwelling causing lower ozone, but this region is also mostly influenced by photo-dissociation from the sunlight, in perpetually sunlit high latitudes. At mid latitudes to high southern latitudes, the red increase in circulation drives higher temperatures from the thermosphere, which increases ozone. This effect is shown by the ozone enhancement in the region. For higher pressures then what is available for MLS, one would expect a ozone depletion in southern high latitudes in JJA above 0.001 hPa. Such a depletion would also correspond with simulation results from Guttu et al. (2020), and would be interesting to analyse for further work using a data set reaching higher than 0.001 hPa.

The residual circulation analysis of high and low Ap shows that EPP affects the circulation in the atmosphere around UMLT, which changes the temperature. The correlation between O_3 and temperature is for the most part positive, which is opposite of what one would expect due to the chemistry. Thus the ozone is being controlled by a combination of transport and temperature effects. Given the correlation plots earlier and the circulation plots in this section, it would appear that the circulation plays a major role. One theory could be that the relative downwelling while increasing temperature and reducing reactivity, is bringing down more reactants for the production of O_3 than for the destruction. To verify this, research on the other reactants in the chemical equilibrium is necessary.

Velocity streamfunction for MAM and SON

Figure 5.15 and 5.16 show the velocity streamfunction given by WACCM for high and low geomagnetic activity for March, April, May (MAM) and September, October, November (SON) respectively. High Ap drives an anomalous circulation cell which connects to the lower thermospheric circulation in southern and northern high latitudes for MAM and

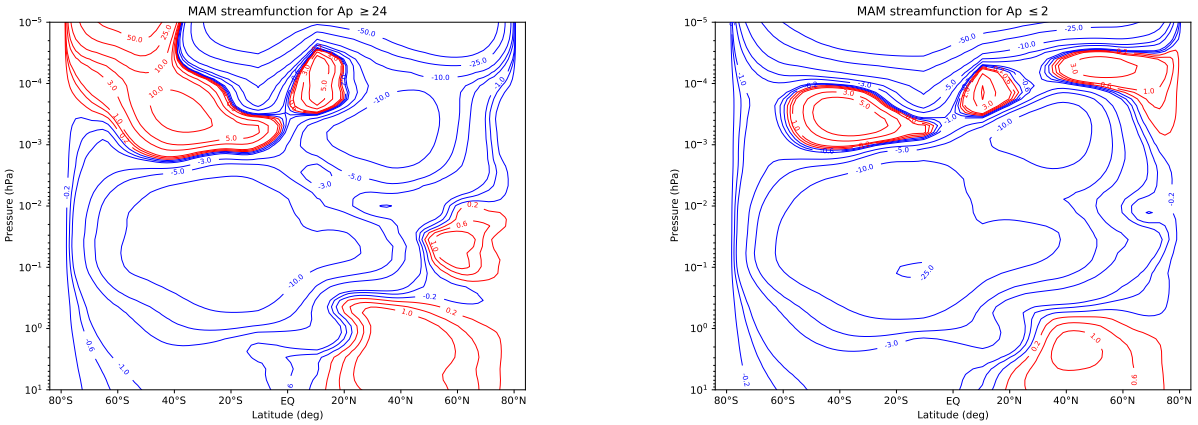

(a) Ap ≥ 24 (b) Ap ≤ 2

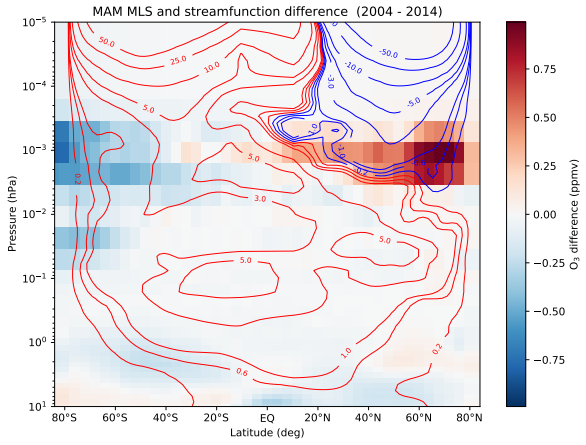

(c) Ap ≥ 24 - Ap ≤ 2

Figure 5.15: Velocity streamfunction from SD-WACCM-X for high and low Ap values in March, April, May (MAM) where red indicates clockwise circulation and blue indicated anti-clockwise circulation. Subfigure 5.13c shows the change in velocity streamfunction (high-low Ap) and the MLS ozone mixing ratio difference for years 2004-2014.

SON respectively. The difference in the high and low geomagnetic activity in the velocity streamfunction is compared to the difference in the MLS ozone mixing ratio in subfigures 5.15c and 5.16c for MAM and SON respectively. The ozone-temperature correlation from figure 5.8 gives a strictly positive correlation for both seasons.

In MAM the difference in circulation from geomagnetic effects is mostly increasing the circulation (red), but Ap still drives an anomalous slow-down in circulation (blue) in the NH for pressure levels at 5×10^{-2} and above. This gives relative downwelling at northern mid-latitudes and relative upwelling at high northern latitudes. The relative downwelling contributes to the higher ozone seen in the northern hemisphere, but the relative upwelling would normally give lower ozone. This might not be the case since in the transitional seasons the MLS nighttime ozone is driven by the seasonal summer to winter pole background.

In SON the difference in circulation shows slow-down in circulation (blue) for the most part, except the anomalous increase in circulation (red) driven by high Ap in the SH. This

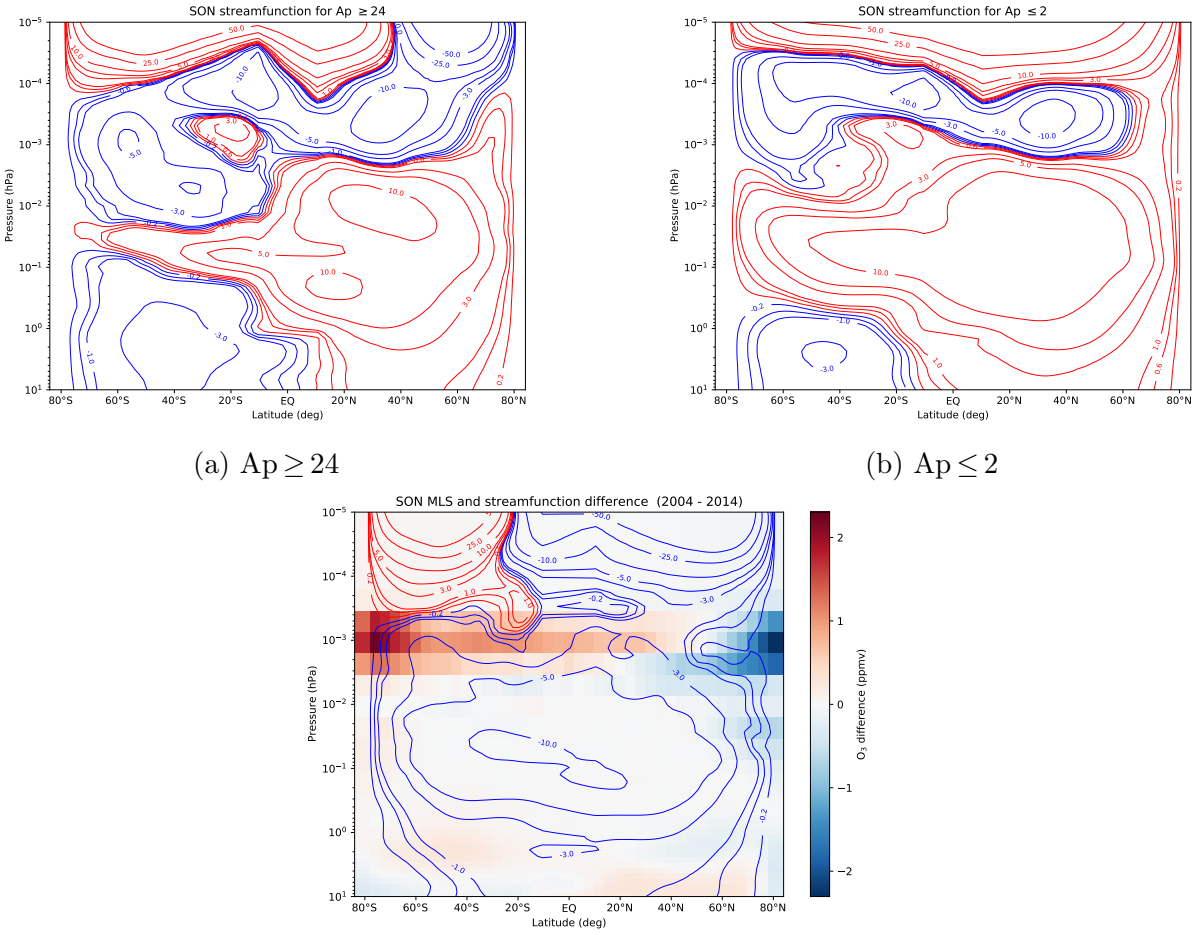

(a) Ap ≥ 24

(b) Ap ≤ 2

(c) Ap ≥ 24 - Ap ≤ 2

Figure 5.16: Velocity streamfunction from SD-WACCM-X for high and low Ap values in September, October, November (SON) where red indicates clockwise circulation and blue indicated anti-clockwise circulation. Subfigure 5.13c shows the change in velocity streamfunction (high-low Ap) and the MLS ozone mixing ratio difference for years 2004-2014.

gives relative downwelling and higher ozone at southern mid-latitudes. At high southern latitudes this should contribute to lower ozone, which is not the case in subfigure 5.16c. This is again due to the seasonal summer to winter pole background flow which dominated the dynamics of the transitional seasons.

In summary, the residual circulation in the UMLT region is affected by EPP. From the circulation plot from all seasons, it appears that circulation plays a major role in the effect of EPP on the secondary ozone layer. To further quantify the full role of circulation one would have to analyse the other sources and sinks of ozone. It would also be of great scientific interest to further analyse the temperature and ozone relationship, perhaps by a seasonal zonal-mean cross-section of temperature compared to the seasonal zonal-mean cross-section of ozone shown in section 5.4. An early attempt of such an analysis is shown in Appendix B.

5.6 Case study of 7-10. November 2004

To assess whether effects of EPP seen in the seasonal zonal-means and the residual circulation is relevant for specific cases, a case study of the geomagnetic event of 7-10. Nov 2004 is conducted. In this section the results of the analysis are shown through zonal-means of ozone mixing ratio, time-series of ozone, CO and temperature at 0.001 hPa for all latitudes and high northern latitudes specifically and maps of the northern hemisphere at different snapshots in time.

Zonal-mean

Figure 5.17 shows the zonal-mean ozone mixing ratio for the snapshots in time before (1-5. Nov 2004), at the event (6-12. Nov 2004), after (13-17. Nov 2004) and longer after (18-22. Nov 2004) and the differences in the ozone mixing ratio around the event is highlighted by O_3 difference maps between the last three snapshots and before the geomagnetic event. The ozone mixing ratio reaches up to ~ 14 ppmv at the secondary ozone layer for the event. At southern high latitudes and expanding into the equator there is a ozone depletion that gets stronger with the passing time. This could be due to dynamical changes in the atmosphere, as ozone slowly move towards the northern pole in the month of November. In the northern hemisphere a tripole of ozone depletion, ozone enhancement and ozone depletion is visible for the upper mesosphere. This ozone variability tripole is strongest for the snapshot of the event - before, and becomes less visible with time. The ozone depletion at 0.02 hPa (~ 74 km) follows previous research about the tertiary ozone layer. The ozone depletion in northern high latitudes at 0.001 hPa shows the same trend as previously shown in the seasonal zonal-means of SON in figure 5.12. The ozone enhancement in between 0.001 hPa and the tertiary ozone layer at 0.02 hPa is not apparent in the SON zonal-mean.

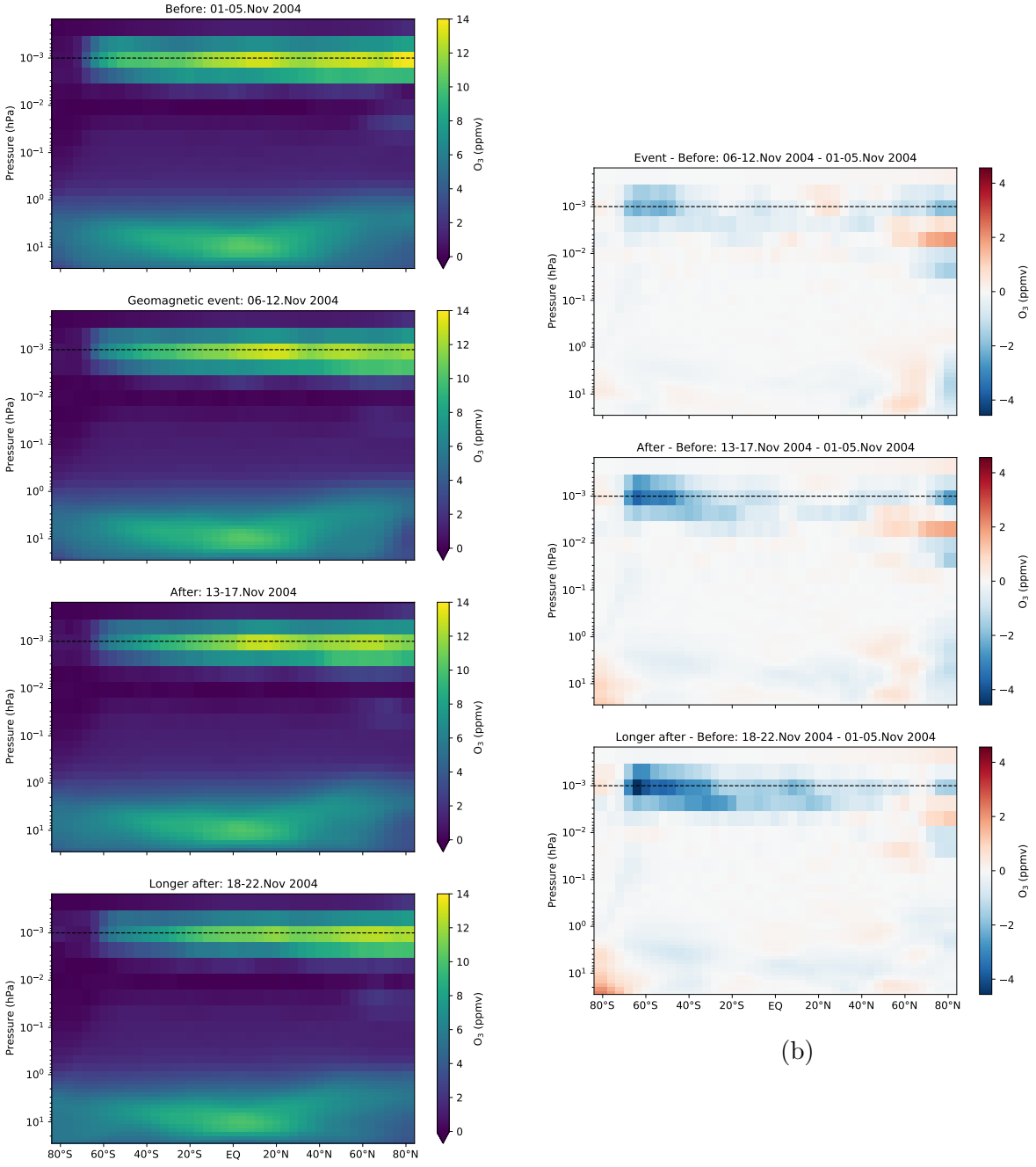

Figure 5.17: Zonal-mean ozone mixing ratio (a) for several snapshots in time around the SPE of 7-10. November 2004 with the difference (b) for each snapshot with the ozone mixing ratio before (1-5. Nov 2004) the event.

Time-series at pressure level 0.001 hPa

To study how the geomagnetic event, and hence EPP, affects secondary ozone with time, a time-series of the month November at pressure level 0.001 hPa is shown in figure 5.18. This shows the temporal changes in MLS nighttime ozone, temperature and nighttime CO

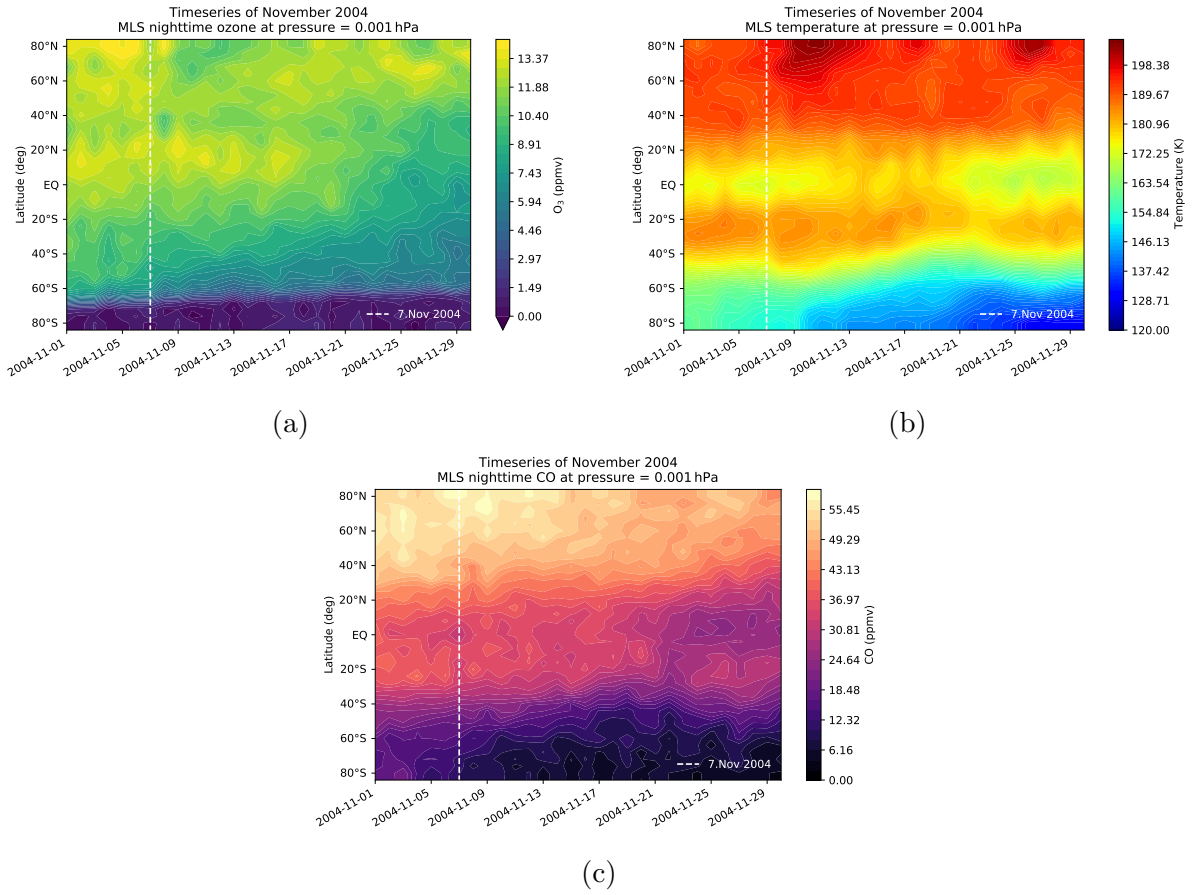

Figure 5.18: Time-series of MLS nighttime ozone (a), MLS temperature (b) and MLS nighttime CO (c) in November 2004. White stippled line indicates 7. Nov 2004, the first day in the Nov 2004 solar proton event.

for all latitudes. The white stippled line indicated 7. Nov 2004, the first day in the Nov 2004 solar proton event. From the zonal-mean cross-sections of the geomagnetic event a small ozone drop is expected at high northern latitudes. At high northern latitudes a slight ozone drop of ~ 3 ppmv and a temperature increase of ~ 10 ppmv is visible around 9. Nov 2004, which is part of the geomagnetic event in the case study (7-10. Nov 2004). The ozone and temperature levels return to previous values around the 15. Nov 2005, which indicates a small shift in ozone and temperature response compared to the days of the event. For all other latitudes and times the changes in O_3 and temperature correspond to the changes in CO which is a tracer for dynamical changes, thus these changes is not due to EPP.

To further study the response of ozone, temperature and CO to the geomagnetic event, a time-series of the northern high latitudes (60-84°N) is compared to the climatology (2005-2020) of each species in figure 5.19. The climatology includes the yearly standard deviation for each day. Figure 5.19 shows that the temperature increase and ozone drop is of significant values. The MLS nighttime CO at the event shows agreement with the climatologial values. The full climatology with yearly standard deviation for ozone, CO and temperature can be found in Appendix A.

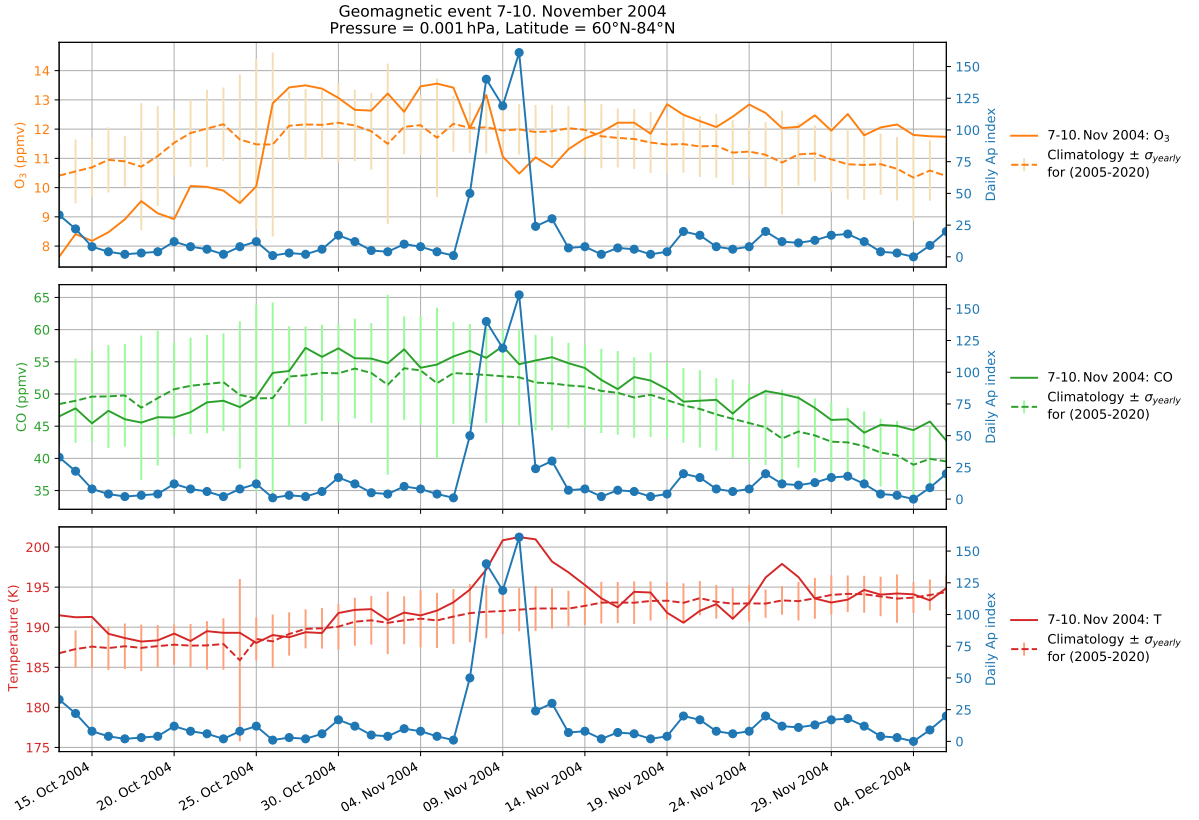

Figure 5.19: Time-series of ozone, CO and temperature before and after the geomagnetic event in Nov 2004 for northern high latitudes (60-84°N) at pressure 0.001 hPa. Stippled line for all species is the climatology (2005-2020) for the given days with yearly standard deviation.

Northern hemisphere maps at pressure level 0.001 hPa

To examine the longitudinal and latitudinal variations in nighttime ozone, temperature and nighttime CO, maps of the northern hemisphere at snapshots in time around the geomagnetic event is analysed. The snapshots consists of before (1-5. Nov 2004), at the event (6-12. Nov 2004), after (13-17. Nov 2004) and longer after (18-22. Nov 2004). When analysing these snapshots its important to know that they are not synoptic snapshots, but rather at a fixed local solar time.

Figure 5.20 shows longitudinal and latitudinal variations in nighttime ozone mixing ratio at 0.001 hPa for snapshots in time before, at, after and longer after the geomagnetic event. The difference maps in subfigure 5.20b highlight the change between the event - before, after - before and longer after - before. For most longitudes in the northern hemisphere the MLS nighttime ozone displays an ozone depletion, as expected from the zonal-mean in figure 5.17 and the time-series from figure 5.18 and 5.19. The exception being a ozone enhancement around Alaska which is at its highest for the after - before difference map, with ozone difference up to about ~ 6 ppmv.

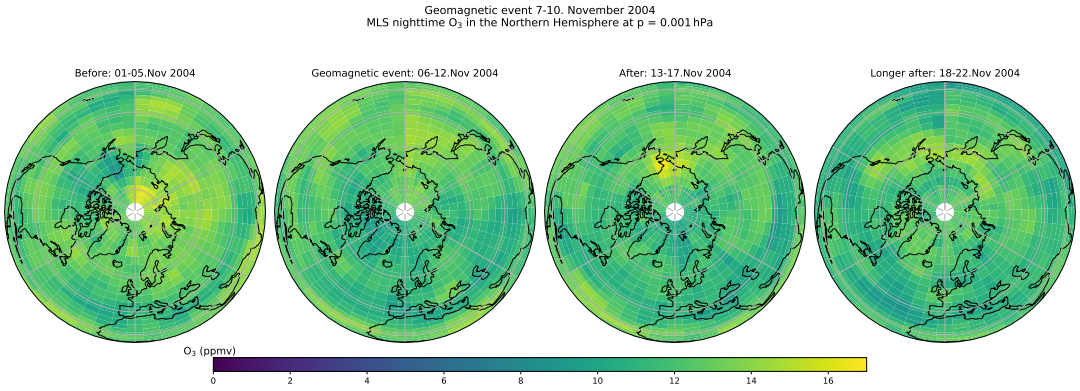

(a)

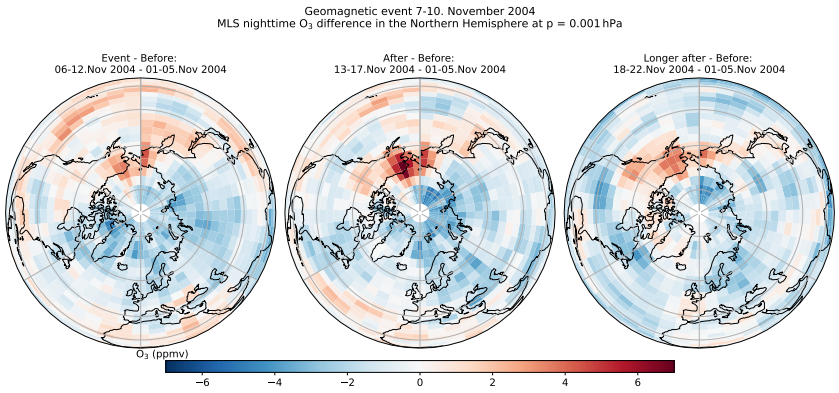

(b)

Figure 5.20: Geographic maps of MLS nighttime ozone at 0.001 hPa (a) for snapshots in time around the geomagnetic event of 7-10. Nov 2004, with the difference (b) in each snapshot compared to before (1-5. Nov 2004) the event.

Figure 5.21 shows longitudinal and latitudinal variations in nighttime CO mixing ratio at 0.001 hPa for snapshots in time before, at, after and longer after the geomagnetic event. The difference maps in subfigure 5.21b highlight the change between the event - before, after - before and longer after - before. The difference between the event - before show both CO enhancement and depletion at high northern latitudes. The slight CO enhancement is not apparent in the difference between longer after - before.

Lastly the longitudinal and latitudinal variations in MLS temperature for the geomagnetic event is displayed in figure 5.22. The geomagnetic event in subfigure 5.22a clearly shows an temperature increase, which is confirmed by the difference map between the event and before in subfigure 5.22b. The increase in temperature is apparent for almost all longitudes, except around Alaska. This corresponds with the findings in figure 5.20.

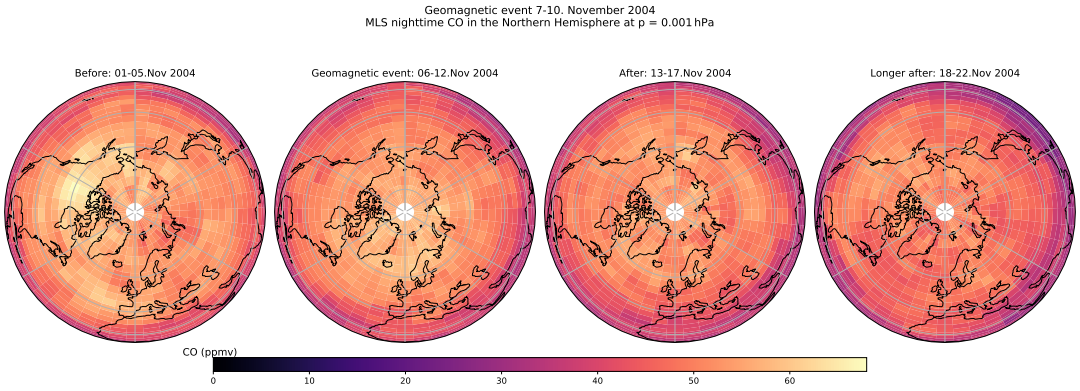

(a)

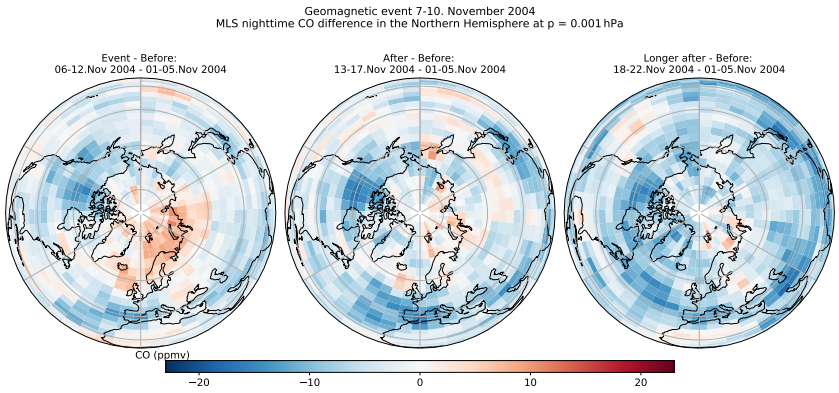

(b)

Figure 5.21: Geographic maps of MLS nighttime CO at 0.001 hPa (a) for snapshots in time around the geomagnetic event of 7-10. Nov 2004, with the difference (b) in each snapshot compared to before (1-5. Nov 2004) the event.

In summary, the maps show that O_3 is a balance between temperature, radical species and species transport. In some areas, such as in Alaska, production species are being transported in faster than destruction species. The gulf of Alaska is known for a characteristic tropospheric high pressure that may have a circulation effect. When analysing the maps one also has to consider the horizontal transport of species, where transport of oxygen rich air from lower sunlit regions into the high latitude winter pole can also create enhanced ozone production.

One of the main point for the whole of this section is the clear EPP effect of higher temperature and thus lower O_3 at high northern latitudes. Furthermore, the agreement between the zonal-mean of the geomagnetic event and the seasonal zonal-mean of SON backs up the ozone variability seen at high northern latitudes. Both the maps and earlier results from the residual circulation from WACCM-X push the theory that O_3 is a balance between temperature, radical species and species transport.

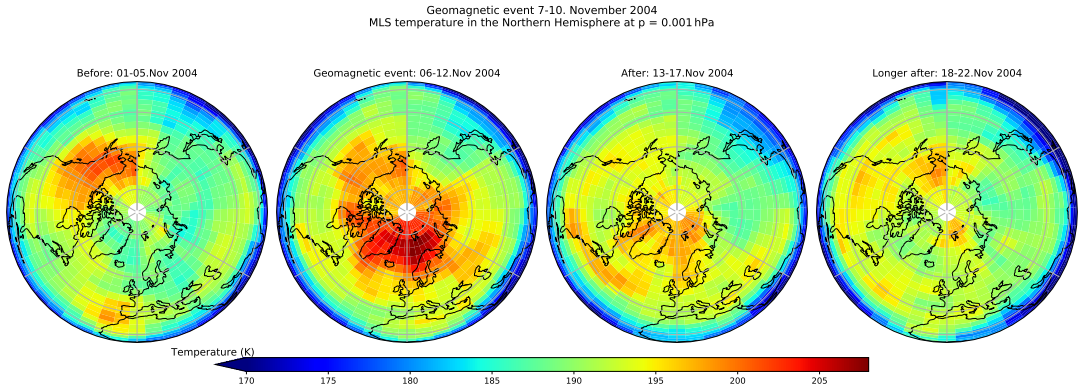

(a)

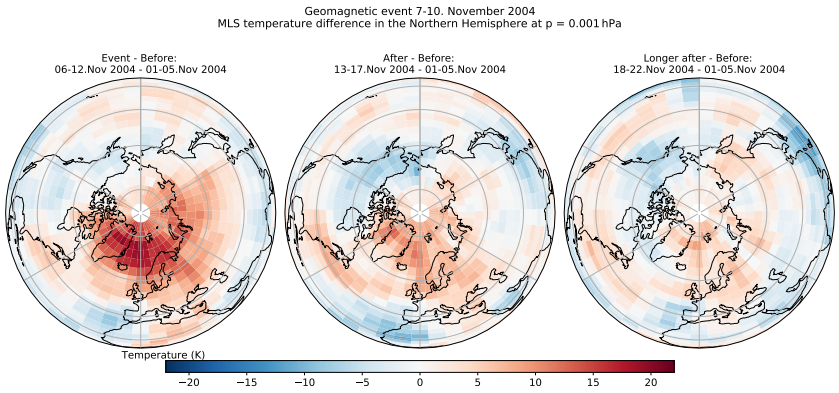

(b)

Figure 5.22: Geographic maps of MLS temperature at 0.001 hPa (a) for snapshots in time around the geomagnetic event of 7-10. Nov 2004, with the difference (b) in each snapshot compared to before (1-5. Nov 2004) the event.

5.7 Superposed Epoch Analysis in DJF

The time-series of the previous section sparked the question of a temporal shift in the effect of EPP on nighttime ozone. A superposed Epoch Analysis in DJF was thus conducted. From seasonal zonal-means in DJF one would expect a small ozone enhancement in DJF at northern latitudes for day 0. Time-series of the geomagnetic event in November on the other hand, indicates a ozone drop a might occur with a small shift in time to day 0, which corresponds to an increase in temperature with the same shift.

The superposed epoch of MLS ozone mixing ratio with high Ap threshold criteria, $\mathrm{Ap} \geq 24$, for day 0 is shown in subfigure 5.23a. The figure shows a slight decrease in O_3 at northern high latitudes after day 0, which is highlighted further by the difference in SEA and the background variability shown in subfigure 5.23c. While this decrease in ozone is visible for the plots, it does not have a significant value outside the 95% confidence interval calculated by the Monte Carlo bootstrapping method.

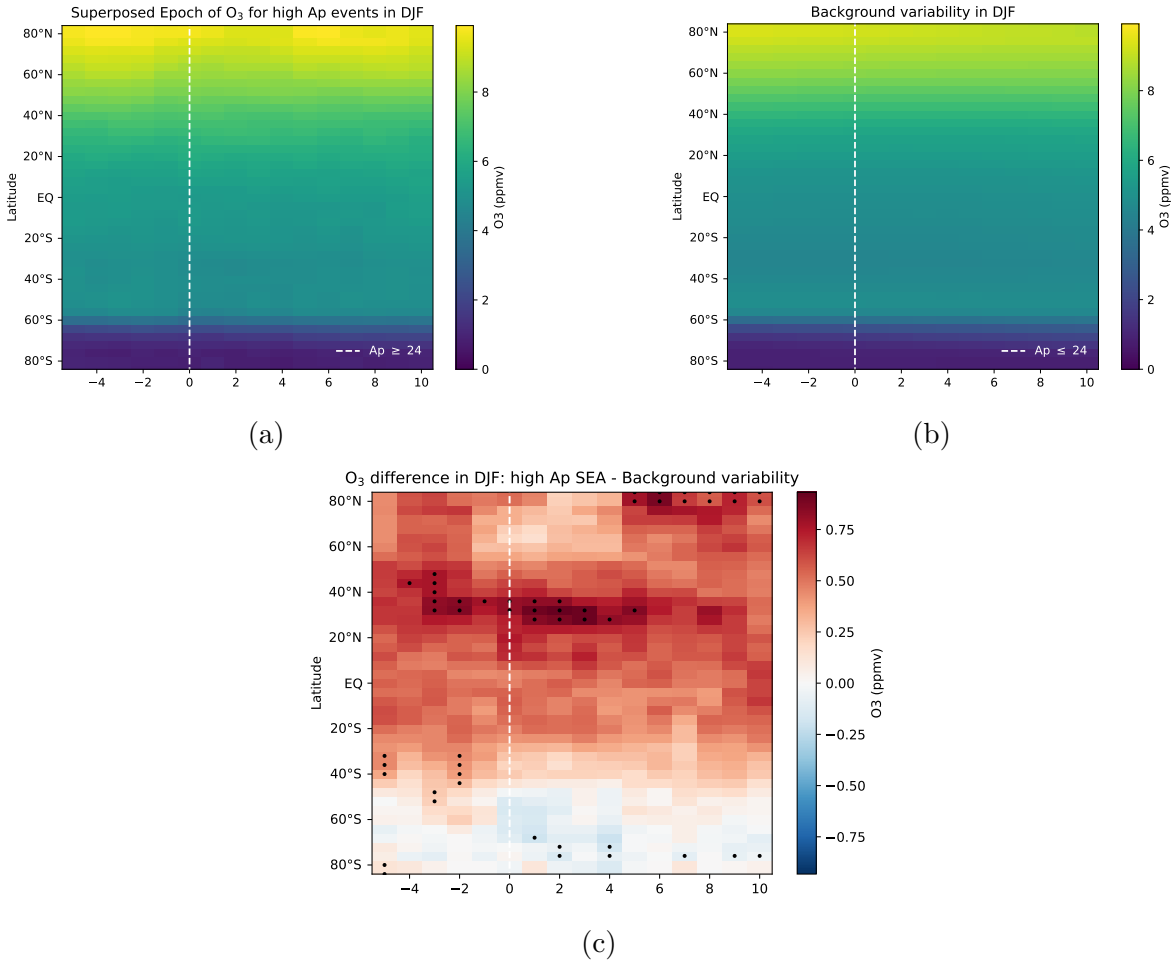

Figure 5.23: MLS O_3 mixing ratio for the superposed epoch of high Ap events (a), the background variability (b) and the difference between the two (c) in DJF with a timeframe of 5 days before and 10 days after the event. Monte Carlo Bootstrapping significance of SEA is highlighted by black dots in the O_3 difference plot.

Figure 5.24 gives the superposed epoch following the high Ap criteria, the background variability and the difference between the two for MLS temperature. Subfigure 5.24a and 5.24c display a slight increase in temperature compared to the surrounding days for northern high latitudes. This is comparable to the decrease in ozone from figure 5.23, and is equally not significant following the MC bootstrapping method for temperature.

In summary, the SEA analysis further strengthens that EPP effects temperature which then affects the ozone variability. Both the ozone and temperature response of geomagnetic activity happens relatively close to the event itself, with a lag of only 1-2 days. As this ozone depletion at high northern latitudes does not correspond directly with the ozone enhancement for the DJF zonal-mean, it raises the question of how the seasonal zonal-means respond to EPP with a lag of 1-2 days. Lastly, its important to point out that at high northern latitudes (60-84°N) neither the ozone enhancement of figure 5.9 or the ozone depletion of figure 5.23c is of significant values.

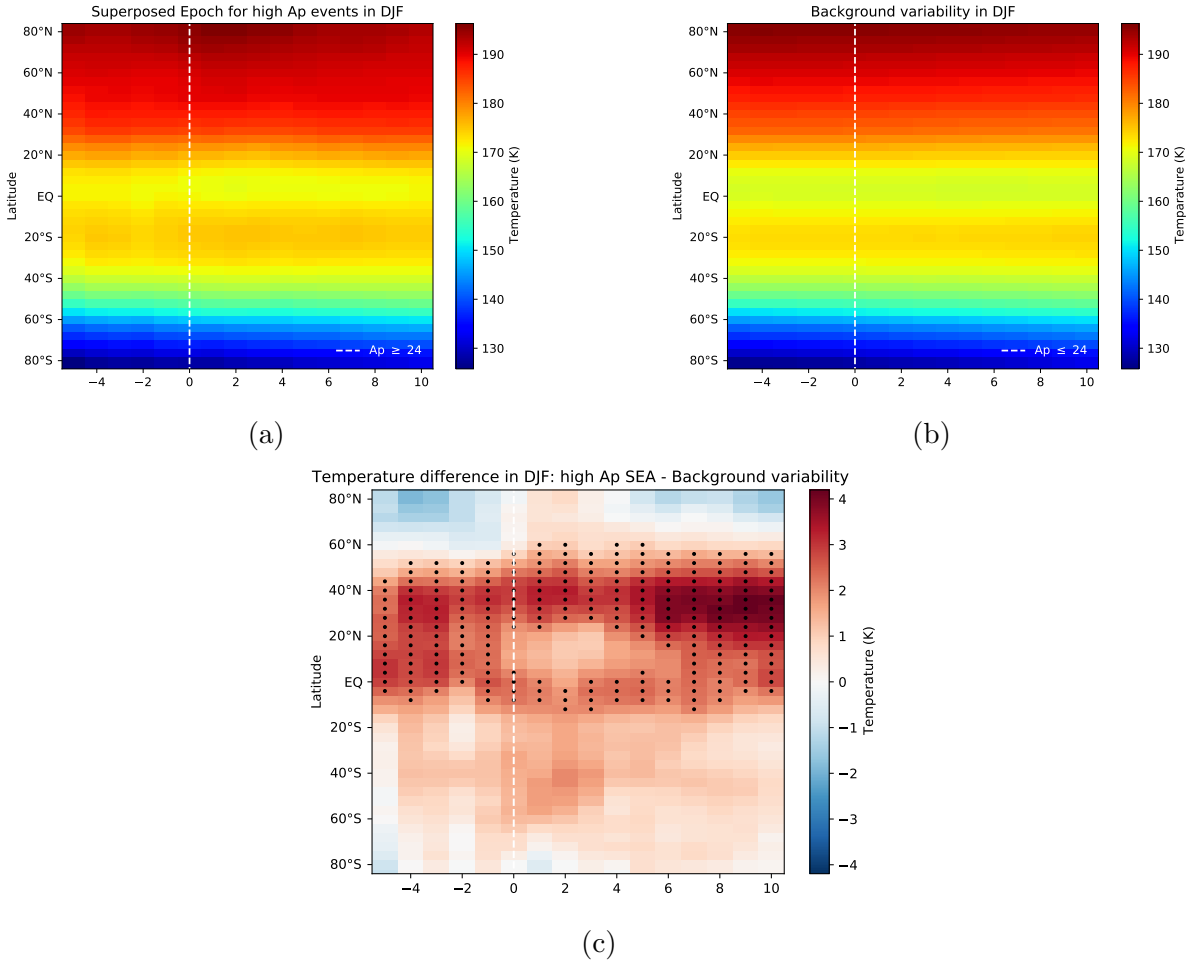

Figure 5.24: MLS temperature for the superposed epoch of high Ap events (a), the background variability (b) and the difference between the two (c) in DJF with a timeframe of 5 days before and 10 days after the event. Monte Carlo Bootstrapping significance of SEA is highlighted by black dots in the temperature difference plot.

Chapter 6

Conclusion and further work

The analysis and results from this thesis show positive results when looking for EPP effects on the secondary ozone layer, where EPP effects on the meridional circulation leads to temperature and composition changes which influence the secondary ozone layer.

The comparison of NASA's Microwave Limb Sounder version 4.2X and version 5.0 show that overall trends in climatology and correlations match. Furthermore, the comparison shows a clear improvement of nighttime ozone and nighttime CO at 0.002 hPa, where the new version have higher O_3 VMR and smoother transitions between months for both species. Thus, deeming MLS V5.0 a good data set to work with for the secondary ozone layer. At the ozone abundance peak at 0.001 hPa, MLS V5.0 have about 20% higher O_3 values than for 0.002 hPa, with both pressure levels showing similar trends for the natural variations due to season, temperature and dynamical effects. Due to the large annual cycle in ozone and CO climatology the effect of EPP gives best results for the high latitude winter regions. Ozone and the dynamical tracer CO are highly correlated, while ozone and temperature is more complex. For most seasons and latitudes the ozone-temperature correlation is positive, except for northern high latitudes in DJF. A positive correlation with temperature is opposite of what is expected from the chemical equilibrium of O_3.

Seasonal zonal-means show an significant ozone enhancement at 0.001 hPa for the DJF and JJA winter season which extends from the polar cap to towards the equator. This significant ozone enhancement is also visible for early spring (March in NH and September in SH) for the MAM and SON zonal-means. In MAM and SON at mid to late autumn an ozone depletion corresponding to simulation results from Guttu et al. (2020) is visible. Results on the residual circulation from SD-WACCM-X show that EPP affects the circulation in the atmosphere around UMLT and that the ozone is being controlled by a combination of transport and temperature effects.

The case study of 7-10. Nov 2004 show that EPP induces higher temperatures and a depletion in ozone at high northern latitudes, which is consistent with seasonal difference in SON zonal-mean ozone VMR. The temperature increase and ozone drop is of significant values compared to yearly standard deviation, and time-series of the event show a small lag in the effect of EPP. Maps of the northern hemisphere show clear correlation between temperature and ozone variability, further pushing the conclusion that the secondary

ozone layer is affected by the changes in temperature, radical species and species transport induces by EPP. The superposed epoch of high Ap events in DJF show a temperature increase and ozone depletion, albeit insignificant, with a lag of 1-2 days relative to the high Ap day itself.

This thesis is one of the first that evaluate EPP influences on the secondary ozone layer through satellite data, and hence there is still much work left. The conclusion that EPP influences the temperature in the circulation around the secondary ozone layer and hence the nighttime ozone, opens for a thorough investigation into EPP influences on temperature and the other sources and sinks of ozone in the secondary layer and a more detailed analysis of the roles of temperature and advection of O_3 sources and sinks for the high Ap conditions. The WACCM-X output (streamfunction, temperature, horizontal and vertical advection) could be used to better understand how the high Ap-induced circulation interacts with the lower thermospheric mean meridional circulation. A place to start with this analysis it to create seasonal zonal-mean cross-sections of temperature and compare to SD-WACCM-X temperature. An example of this is available in Appendix B. Furthermore, as ozone abundance is closely related to atomic oxygen and atomic hydrogen, the influence of these variables would contribute to understanding the effect of EPP on UMLT ozone. Lastly, high Ap events tend to be more abundant during the declining phase of a solar cycle, so further work is needed to better discriminate between the roles of the solar cycle and Ap (i.e. if the 49 events in DJF is oversampling one particular phase). Effects from the solar cycle can be investigated by looking at the solar radio flux given by the F10.7 index.

Appendix A

Yearly standard deviation for 60-80°N climatology at 0.001 hPa

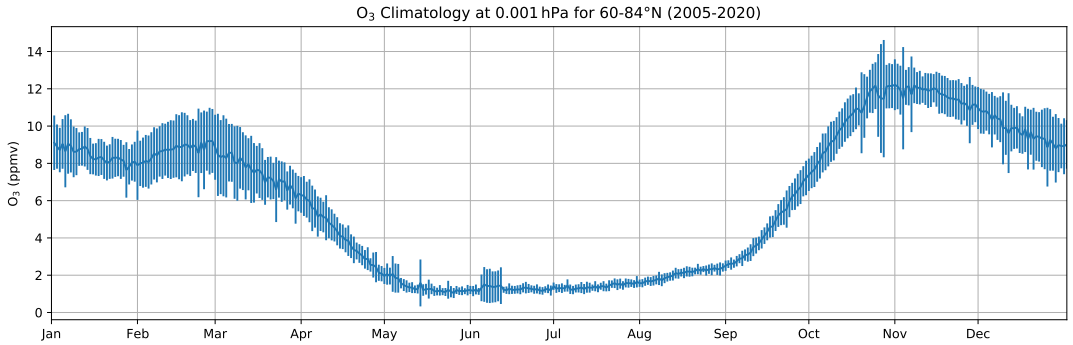

Figure A.1: MLS V5.0 nighttime O_3 climatology with yearly standard deviation for 2005-2020 at pressure 0.001 hPa for 60-84°N.

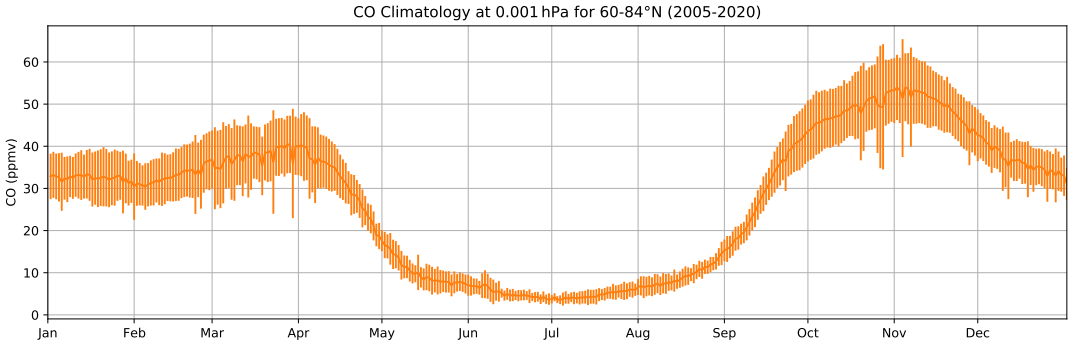

Figure A.2: MLS V5.0 nighttime CO climatology with yearly standard deviation for 2005-2020 at pressure 0.001 hPa for 60-84°N.

The climatology at pressure level 0.001 hPa for northern high latitudes (60-84°N) with the yearly standard deviation retrieved for years 2005-2020 is shown for ozone, CO and temperature in figure A.1, figure A.2 and figure A.3, respectively. This climatology with yearly standard deviation is used in section 5.6 (Case study of 7-10. November 2004) for

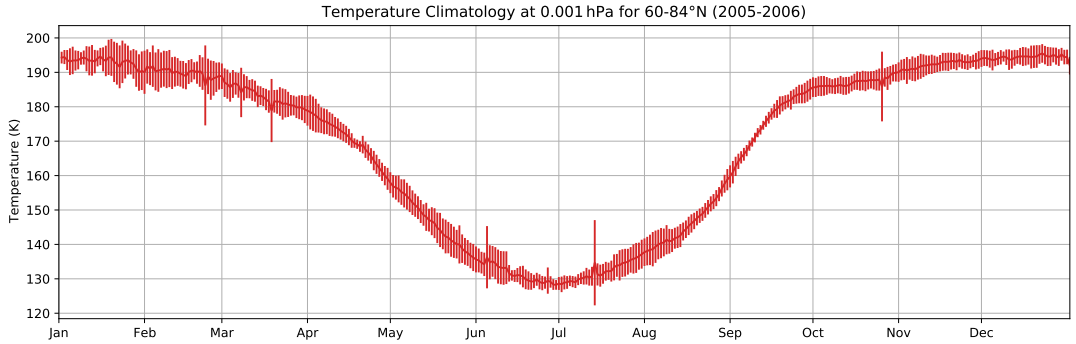

Figure A.3: MLS V5.0 Temperature climatology with yearly standard deviation for 2005-2020 at pressure 0.001 hPa for 60-84°N.

figure 5.19 (Time-series at northern latitudes). For ozone in figure A.1, the yearly standard variation, σ_{yearly}, is about 1-2 ppmv in the winter and less than 0.5 ppmv for most days during summer. For carbon monoxide in figure A.2, σ_{yearly} is about 5-7 ppmv in summer and 1-2 ppmv in winter. The yearly standard variation for temperature in figure A.3 at high latitudes is fairly constant throughout the year, with values between 1-6 K.

Appendix B

Preliminary analysis of temperature

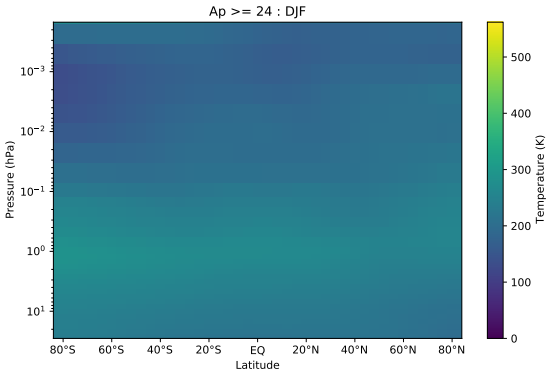

(a) MLS V5.0 Temperature for Ap $\geq$ 24

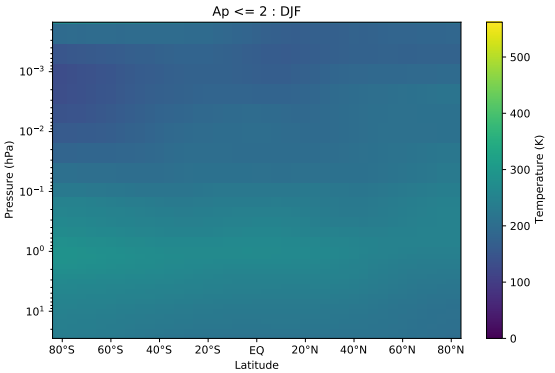

(b) MLS V5.0 Temperature for Ap $\leq$ 2

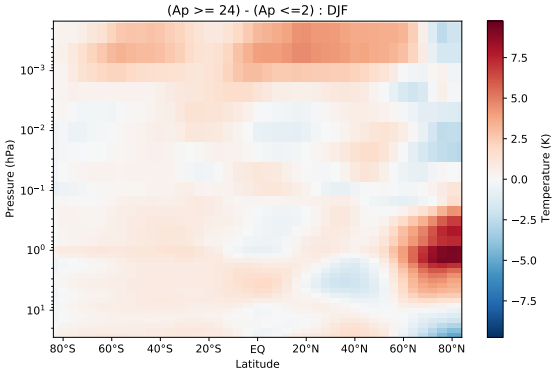

(c) MLS V5.0 Temperature difference

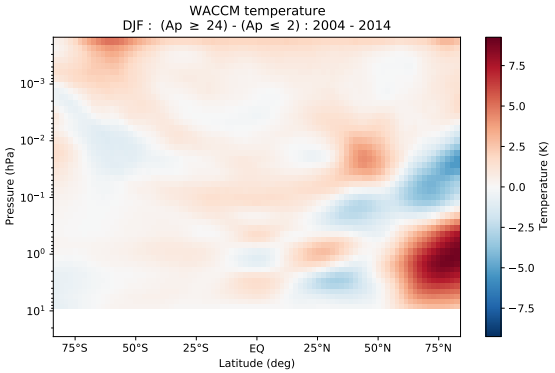

(d) SD-WACCM-X Temperature difference

Figure B.1: Zonal-mean of MLS V5.0 temperature for high Ap and low Ap in DJF. The difference in temperature given by high and low Ap index for both MLS V5.0 and SD-WACCM-X.

Figure B.1 shows the DJF zonal-mean of MLS V5.0 temperature for high Ap and low Ap given by the Ap conditions from subsection 4.2. Subfigure B.1c shows the difference in MLS V5.0 temperature for high Ap subtracted by low Ap, while subfigure B.1d shows the SD-WACCM-X temperature difference given by high and low Ap.

Bibliography

Aikin, A. C. & Smith, H. J. P. (1999). Mesospheric constituent variations during electron precipitation events. *Journal of Geophysical Research: Atmospheres*, *104*(D21), 26457–26471. https://doi.org/https://doi.org/10.1029/1999JD900752

Andrews, D. G. (2010). *An introduction to atmospheric physics* (2nd ed.). Cambridge University Press. https://doi.org/10.1017/CBO9780511800788

Bartels, J. (1949). The standardized index, ks, and the planetary index, kp. *IATME Bull.*, *12b*, 97–120.

Baumgaertner, A., Jöckel, P., Kerkweg, A., Sander, R. & Tost, H. (2016). Implementation of the community earth system model (cesm) version 1.2.1 as a new base model into version 2.50 of the messy framework. *Geoscientific Model Development*, *9*, 125–135. https://doi.org/10.5194/gmd-9-125-2016

Bönisch, H., Engel, A., Birner, T., Hoor, P., Tarasick, D. W. & Ray, E. A. (2011). On the structural changes in the brewer-dobson circulation after 2000. *Atmospheric Chemistry and Physics*, *11*(8), 3937–3948. https://doi.org/10.5194/acp-11-3937-2011

Efron, B. (1979). Bootstrap methods: Another look at the jackknife. *The Annals of Statistics*, *7*(1), 1–26. Retrieved June 16, 2022, from http://www.jstor.org/stable/2958830

Efron, B. & Tibshirani, R. (1995). An introduction to the bootstrap. *Journal of The Royal Statistical Society Series A-statistics in Society*, *158*, 347–347.

Forbes, J. M. (2007). Dynamics of the thermosphere. *Journal of the Meteorological Society of Japan. Ser. II*, *85B*, 193–213. https://doi.org/10.2151/jmsj.85B.193

Gelaro, R., McCarty, W., Suárez, M. J., Todling, R., Molod, A., Takacs, L., Randles, C. A., Darmenov, A., Bosilovich, M. G., Reichle, R., Wargan, K., Coy, L., Cullather, R., Draper, C., Akella, S., Buchard, V., Conaty, A., da Silva, A. M., Gu, W., … Zhao, B. (2017). The modern-era retrospective analysis for research and applications, version 2 (merra-2). *Journal of Climate*, *30*(14), 5419–5454. https://doi.org/10.1175/JCLI-D-16-0758.1

Guttu, S., Orsolini, Y., Stordal, F., Limpasuvan, V. & Marsh, D. R. (2020). Waccm simulations: Decadal winter-to-spring climate impact on middle atmosphere and troposphere from medium energy electron precipitation. *Journal of Atmospheric and Solar-Terrestrial Physics*, *209*, 105382. https://doi.org/https://doi.org/10.1016/j.jastp.2020.105382

Haurwitz, M. W. & Brier, G. W. (1981). A critique of the superposed epoch analysis method: Its application to solar–weather relations. *Monthly Weather Review*, *109*(10), 2074–2079. https://doi.org/10.1175/1520-0493(1981)109⟨2074:ACOTSE⟩2.0.CO;2

Hocke, K. (2017). Response of the middle atmosphere to the geomagnetic storm of november 2004. *Journal of Atmospheric and Solar-Terrestrial Physics*, *154*, 86–91. https://doi.org/https://doi.org/10.1016/j.jastp.2016.12.013

Jackman, C. H., Deland, M. T., Labow, G. J., Fleming, E. L. & López-Puertas, M. (2006). Satellite measurements of middle atmospheric impacts by solar proton events in solar cycle 23. *Space Science Reviews*, *125*. https://doi.org/0.1007/s11214-006-9071-4

Laken, B.A. & Calogovi´c, J. (2013). Composite analysis with monte carlo methods: An example with cosmic rays and clouds. *J. Space Weather Space Clim.*, *3*, A29. https://doi.org/10.1051/swsc/2013051

Lee, J. N., Cahalan, R. F. & Wu, D. L. (2016). Solar rotational modulations of spectral irradiance and correlations with the variability of total solar irradiance. *J. Space Weather Space Clim.*, *6*, A33. https://doi.org/10.1051/swsc/2016028

Lee, J. N. & Wu, D. L. (2020). Solar cycle modulation of nighttime ozone near the mesopause as observed by mls. *Earth and Space Science*, *7*(4). https://doi.org/10.1029/2019EA001063

Lee, J. N., Wu, D. L., Ruzmaikin, A. & Fontenla, J. (2018). Solar cycle variations in mesospheric carbon monoxide. *Journal of Atmospheric and Solar-Terrestrial Physics*, *170*, 21–34. https://doi.org/https://doi.org/10.1016/j.jastp.2018.02.001

Liu, H.-L., Bardeen, C. G., Foster, B. T., Lauritzen, P., Liu, J., Lu, G., Marsh, D. R., Maute, A., McInerney, J. M., Pedatella, N. M., Qian, L., Richmond, A. D., Roble, R. G., Solomon, S. C., Vitt, F. M. & Wang, W. (2018). Development and validation of the whole atmosphere community climate model with thermosphere and ionosphere extension (waccm-x 2.0). *Journal of Advances in Modeling Earth Systems*, *10*(2), 381–402. https://doi.org/https://doi.org/10.1002/2017MS001232

Liu, H.-L., Foster, B. T., Hagan, M. E., McInerney, J. M., Maute, A., Qian, L., Richmond, A. D., Roble, R. G., Solomon, S. C., Garcia, R. R., Kinnison, D., Marsh, D. R., Smith, A. K., Richter, J., Sassi, F. & Oberheide, J. (2010). Thermosphere extension of the whole atmosphere community climate model. *Journal of Geophysical Research: Space Physics*, *115*(A12). https://doi.org/https://doi.org/10.1029/2010JA015586

Lockwood, M., Owens, M., Barnard, L., Scott, C., Watt, C. & Bentley, S. (2018). Space climate and space weather over the past 400 years: 2. proxy indicators of geomagnetic storm and substorm occurrence. *Journal of Space Weather and Space Climate*, *8*. https://doi.org/10.1051/swsc/2017048

Marsh, D. R., Mills, M. J., Kinnison, D. E., Lamarque, J.-F., Calvo, N. & Polvani, L. M. (2013). Climate change from 1850 to 2005 simulated in cesm1(waccm). *Journal of Climate*, *26*(19), 7372–7391. https://doi.org/10.1175/JCLI-D-12-00558.1

Matzka, J., Bronkalla, O., Tornow, K., Elger, K. & Stolle, C. (2021). Geomagnetic kp index. v. 1.0. gfz data services. https://doi.org/https://doi.org/10.5880/Kp.0001

Matzka, J., Stolle, C., Yamazaki, Y., Bronkalla, O. & Morschhauser, A. (2021). The geomagnetic kp index and derived indices of geomagnetic activity [e2020SW002641 2020SW002641]. *Space Weather*, *19*(5), e2020SW002641. https://doi.org/https://doi.org/10.1029/2020SW002641

Menvielle, M., Iyemori, T., Marchaudon, A. & Nosé, M. (2010). Geomagnetic indices. *Geomagnetic observations and models* (pp. 183–228). Springer Netherlands. https://doi.org/10.1007/978-90-481-9858-0_8

Mironova, I., Aplin, K., Arnold, F., Bazilevskaya, G., Harrison, R., Krivolutsky, A., Nicoll, K., Rozanov, E., Turunen, E. & Usoskin, I. (2015). Energetic particle influence on the earth's atmosphere. *Space Science Reviews*, *194*. https://doi.org/10.1007/s11214-015-0185-4

NASA Goddard. (n.d.). *About aura*. Retrieved June 17, 2022, from https://aura.gsfc.nasa.gov/about.html

NASA Jet Propulstion Laboratory. (n.d.). *Aura mls*. Retrieved June 17, 2022, from https://mls.jpl.nasa.gov/eos-aura-mls

Panasenko, S. V. & Chernogor, L. F. (2007). Event of the november 7–10, 2004, magnetic storm in the lower ionosphere. *Geomagnetism and Aeronomy*, *47*, 608–620. https://doi.org/10.1134/S0016793207050106

Qian, L., Burns, A. G., Emery, B. A., Foster, B., Lu, G., Maute, A., Richmond, A. D., Roble, R. G., Solomon, S. C. & Wang, W. (2014). The ncar tie-gcm. *Modeling the ionosphere–thermosphere system* (pp. 73–83). American Geophysical Union (AGU). https://doi.org/https://doi.org/10.1002/9781118704417.ch7

Rastogi, R., Chandra, H., Condori, L., Abdu, M., Reinisch, B., Tsunoda, R., Prasad, D., Pant, T. & Maruyama, T. (2012). Abnormally large magnetospheric electric field on 9 november 2004 and its effect on equatorial ionosphere around the world. *Journal of Earth System Science*, *121*, 1145–1161. https://doi.org/10.1007/s12040-012-0231-5

Ratick, S. & Schwarz, G. (2009). Monte carlo simulation. In R. Kitchin & N. Thrift (Eds.), *International encyclopedia of human geography* (pp. 175–184). Elsevier. https://doi.org/https://doi.org/10.1016/B978-008044910-4.00476-4

Rostoker, G. (1972). Geomagnetic indices. *Reviews of Geophysics*, *10*(4), 935–950. https://doi.org/https://doi.org/10.1029/RG010i004p00935

Schwartz, M., Froidevaux, L., Livesey, N., Read, W. & Fuller, R. (2021). Mls/aura level 3 daily binned ozone (o3) mixing ratio on assorted grids v005. https://doi.org/https://doi.org/10.5067/Aura/MLS/DATA/3516

Simi, K. G., Manju, G., Haridas, M. K. M., Nayar, S. R. P., Pant, T. K. & Alex, S. (2013). Ionospheric response to a geomagnetic storm during november 8–10, 2004. *Earth, Planets and Space*, *65*, 343–350.

Smith, A. K. & Marsh, D. R. (2005). Processes that account for the ozone maximum at the mesopause. *Journal of Geophysical Research: Atmospheres*, *110*(D23). https://doi.org/10.1029/2005JD006298

Solomon, S., Garcia, R. R., Olivero, J. J., Bevilacqua, R. M., Schwartz, P. R., Clancy, R. T. & Muhleman, D. O. (1985). Photochemistry and transport of carbon monoxide in the middle atmosphere. *Journal of Atmospheric Sciences*, *42*(10), 1072–1083. https://doi.org/10.1175/1520-0469(1985)042⟨1072:PATOCM⟩2.0.CO;2

Yermolaev, Y., Zelenyi, L., Kuznetsov, V., Chertok, I., Panasyuk, M., Myagkova, I., Zhitnik, I., Kuzin, S., Eselevich, V., Bogod, V., Arkhangelskaja, I., Arkhangelsky, A. & Kotov, Y. (2008). Magnetic storm of november, 2004: Solar, interplanetary, and magnetospheric disturbances [Recent Observations and Simulations of the Sun-Earth System]. *Journal of Atmospheric and Solar-Terrestrial Physics*, *70*(2), 334–341. https://doi.org/https://doi.org/10.1016/j.jastp.2007.08.020

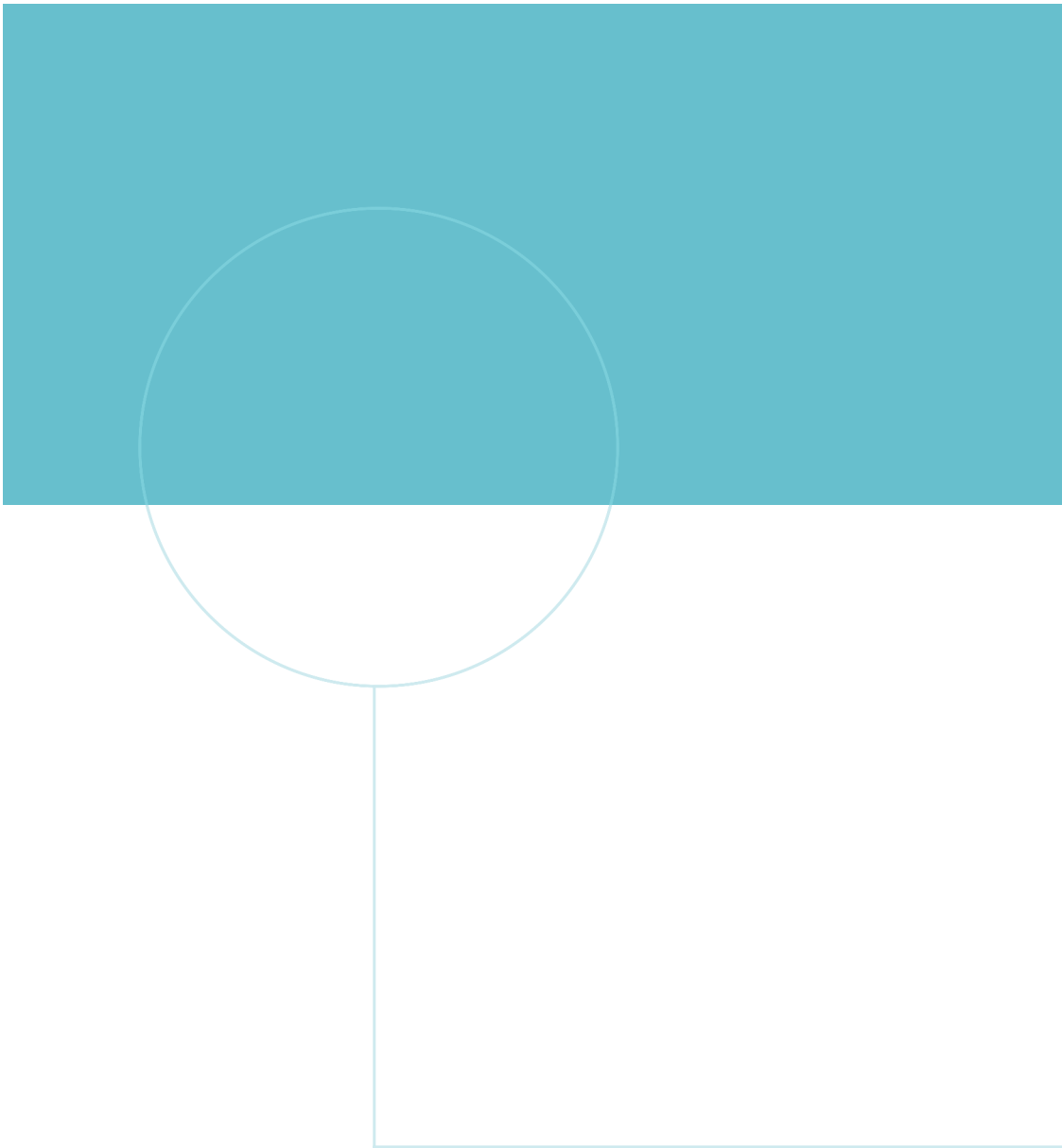

NTNU

Norwegian University of
Science and Technology